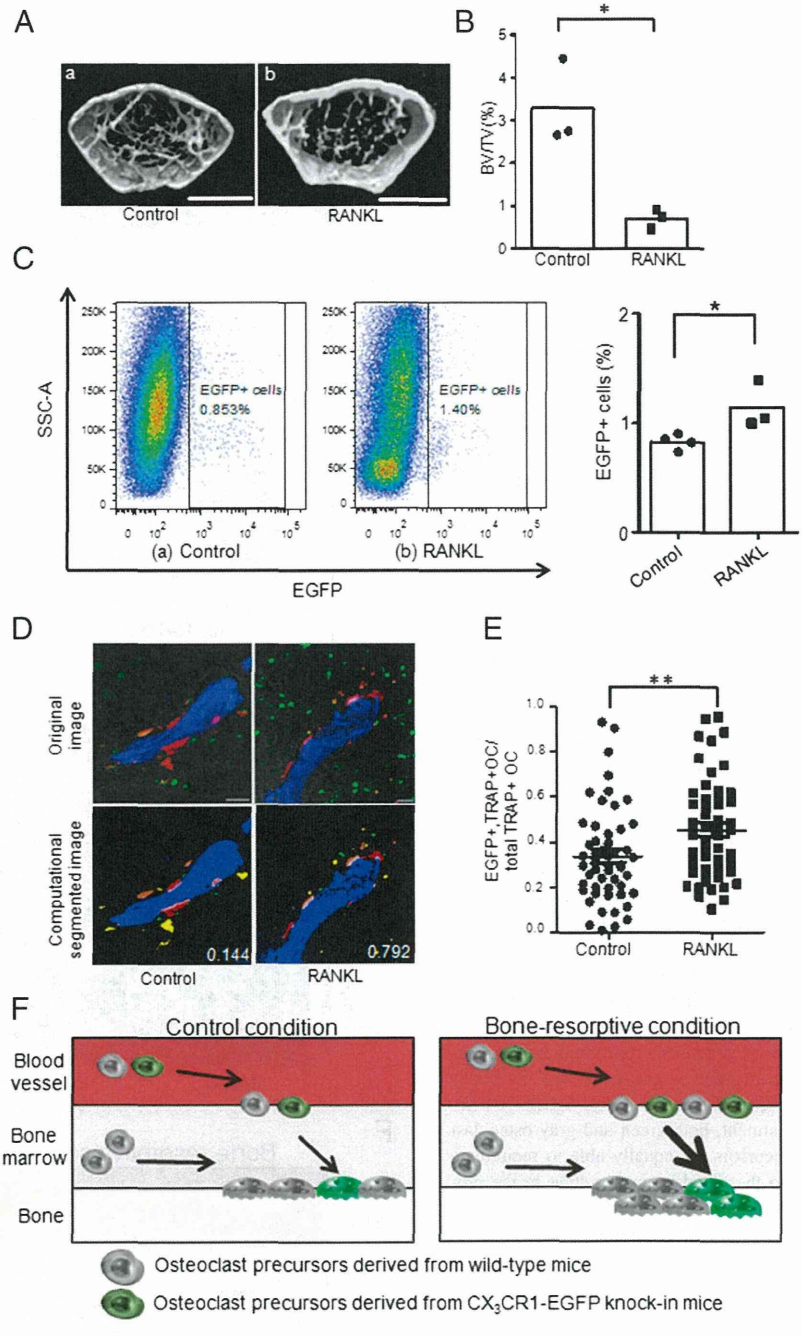

FIGURE 2. Mobilization of circulating osteoclast precursors under bone-resorptive conditions. (**A**) Characterization of the RANKL-induced bone loss model. Femurs were collected from wild-type mice after RANKL was i.p. injected (20 μg/pair) for 2 d (**b**). Control parabiotic pairs were injected with saline only (**a**). Scale bars, 1 mm. (**B**) Bone samples were measured by cone-beam μCT. BV/TV (%) was calculated from μCT images. $*p < 0.05$ (two-tailed unpaired t test). (**C**) Flow cytometric analyses of bone marrow cells collected from wild-type mice connected with CX_3CR1-EGFP knock-in mice after i.p. injection of saline (**a**) or RANKL (**b**) ($n = 4$ and $n = 3$, respectively). $*p < 0.05$ (two-tailed unpaired t test). (**D**) Histological examination combined with computational analysis to measure the length of the white line. *Upper panels*, original images; *lower panels*, segmented images. Blue area, bone trabeculae (second harmonic fluorescent signal); orange and yellow area, $EGFP^+$ $TRAP^+$ osteoclasts attached to or detached from bone trabeculae, respectively; red and green area, $TRAP^+$ osteoclasts attached to or detached from bone trabeculae; white line, osteoclast and bone attachment interface. The $EGFP^+$ $TRAP^+$ osteoclast/total $TRAP^+$ osteoclast ratios are indicated by white numbers. Scale bars, 30 μm. (**E**) Proportion of $TRAP^+$ osteoclasts that were $EGFP^+$. Data represent the mean ± SEM ($n = 52$). $**p < 0.01$ (two-tailed unpaired t test). (**F**) Schematic illustration of osteoclast precursor mobilization. Osteoclast precursors can be generated from circulating monocytes (green + gray), as well as bone-resident precursors (gray). Under bone-resorptive conditions, recruitment of circulating monocytes into bones is increased, leading to an increase in proportion of osteoclasts on the bone surface that are positive for EGFP (green).

prevent loss of bone density during ovariectomy-induced osteoporosis (14). We induced osteoclastic bone resorption in parabiotic mouse pairs through i.p. injection of RANKL (20 μg/pair) and further administered FTY720 (3 mg/kg) or vehicle in 24-h intervals to test their therapeutic effects (Fig. 3A). The jointed pairs were killed 48 h after the last injection, and we confirmed that the bone mineral density, defined as the BV/TV ratio (%), was significantly increased in FTY720-treated wild-type mice (Fig. 3B), as observed in the ovariectomy model (14). We also demonstrated that the total number of $EGFP^+$ cells in bone marrow was significantly decreased by FTY720 treatment (Fig. 3C), which is also consistent with the literature (14).

We performed immunofluorescence analysis of bone sections from mice treated with RANKL with or without FTY720 (Fig. 3D). Although the total number of bone-lining osteoclasts was significantly decreased in mice treated with FTY720 (14), the proportion of osteoclasts that were $EGFP^+$ did not differ significantly between the two groups (Fig. 3E). These results suggest that $EGFP^-$ osteoclast precursors generated in wild-type bone marrow and $EGFP^+$ precursors originally derived from CX_3CR1-EGFP knock-in mouse bones and homed into wild-type bone marrow have comparable abilities to recirculate into the bloodstream after application of FTY720. However, we could not completely exclude the possibility that FTY720 may influence the differentiation of osteoclasts (Fig. 3F).

Tracking the movement of osteoclast precursors in photoconvertible fluorescence protein "KikGR" knock-in mice

To clarify whether osteoclast precursors were really circulating, we also used a different technique involving the photoconvertible fluorescent protein KikGR. We applied this method to study dynamic cell behavior using mouse strains in which KikGR is

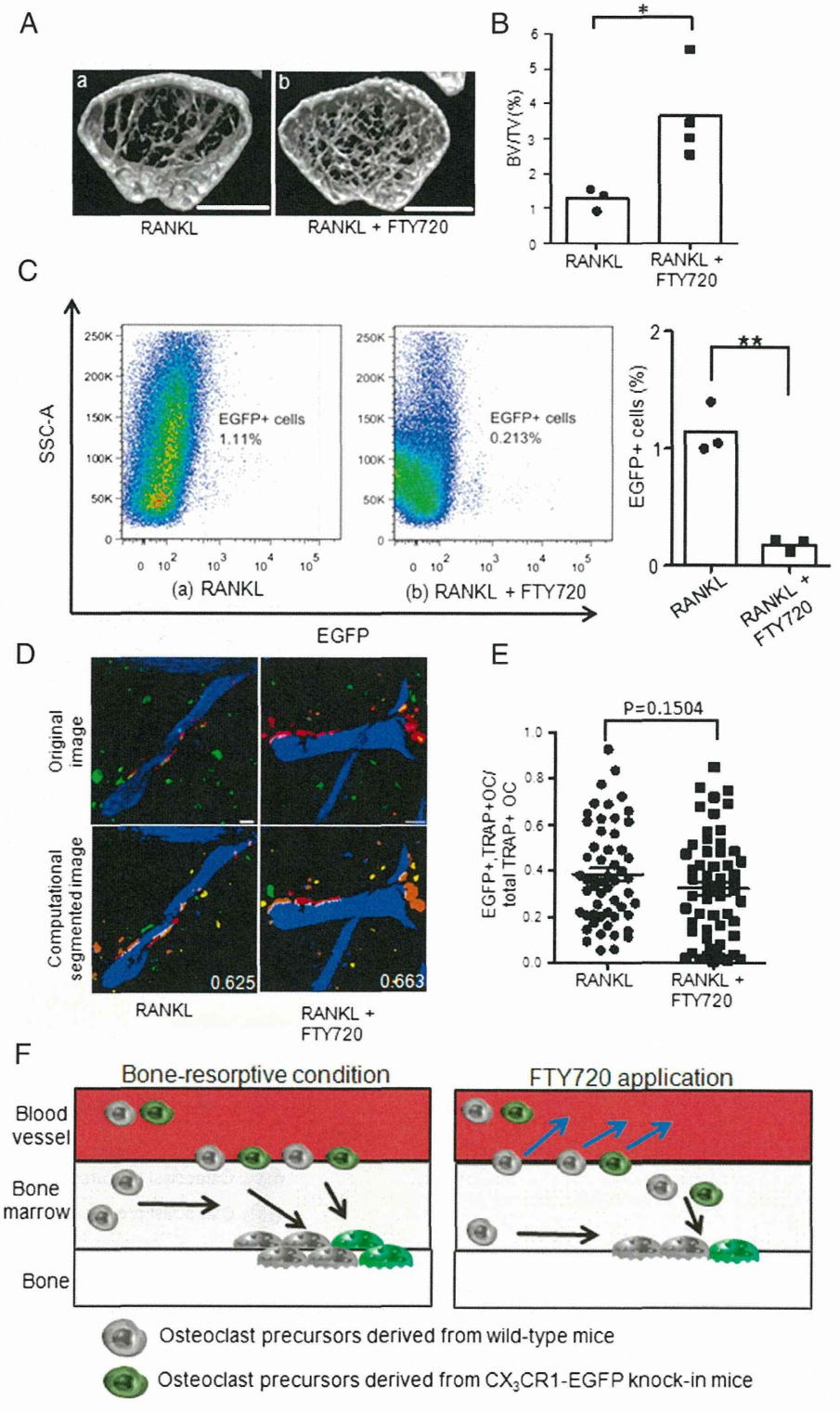

FIGURE 3. Mobilization of circulating osteoclast precursors under bone-treatment conditions. (**A**) Characterization of the effect of FTY720 administration. Femurs were collected from wild-type mice after i.p. injection of RANKL + vehicle ($n = 3$) (**a**). FTY720-treated parabiotic pairs were injected with RANKL + FTY720 ($n = 4$) (**b**). Scale bars, 1 mm. (**B**) Bone samples were analyzed by cone-beam μCT. BV/TV (%) was calculated from μCT images. $*p < 0.05$ (two-tailed unpaired t test). (**C**) Flow cytometric analyses of bone marrow cells collected from RANKL-treated (**a**) and RANKL + FTY720-treated (**b**) mice ($n = 3$). $**p < 0.01$ (two-tailed unpaired t test). (**D**) Histological examination combined with computational analysis to measure the length of the white line. *Upper panels*, original images; *lower panels*, computational segmented images. The $EGFP^+$ $TRAP^+$ osteoclast/total $TRAP^+$ osteoclast ratios are indicated by white numbers. Scale bars, 30 μm. (**E**) Proportion of $TRAP^+$ osteoclasts that were $EGFP^+$. Data represent the mean ± SEM ($n = 55$ for RANKL and $n = 58$ for RANKL + FTY720). (**F**) Schematic illustration of FTY720-induced recirculation of osteoclast precursors. Osteoclast precursors can be generated from circulating monocytes (green + gray), as well as bone-resident precursors (gray). After FTY720 treatment, both green and gray osteoclast precursors are equally able to recirculate into the bloodstream, resulting in the proportion of osteoclasts that are positive for EGFP (green) being unaltered.

expressed in osteoclast precursors. We generated RANK-KikGR mice by crossing ROSA-CAG-lox-stop-lox-KikGR knock-in mice with RANK-Cre knock-in mice. RANK is a cognate receptor for RANKL, which is required for differentiation into mature osteoclasts (31). Bone marrow cells from RANK-KikGR mice were analyzed by flow cytometry (Fig. 4A). We confirmed that 0.659 ± 0.16% (mean ± SEM; $n = 3$) of all bone marrow cells expressed KikGR, and that $KikGR^+$ cells could differentiate into $TRAP^+$ osteoclast-like cells in vitro (Fig. 4B). Furthermore, Rank mRNA expression was higher in $KikGR^+$ cells than in $KikGR^-$ cells (Fig. 4C), indicating that some $KikGR^+$ cells in RANK-KikGR mice are osteoclast precursors.

We evaluated the efficiency of photoconversion of KikGR expressed in $RANK^+$ cells in single-cell suspensions. Splenocytes from RANK-KikGR mice exposed to violet light (436 nm) for 10 min exhibited red-shifted emission signals compared with non-exposed cells (Fig. 4D), indicating successful photoconversion under this condition. Next, we assessed the photoconversion ef-

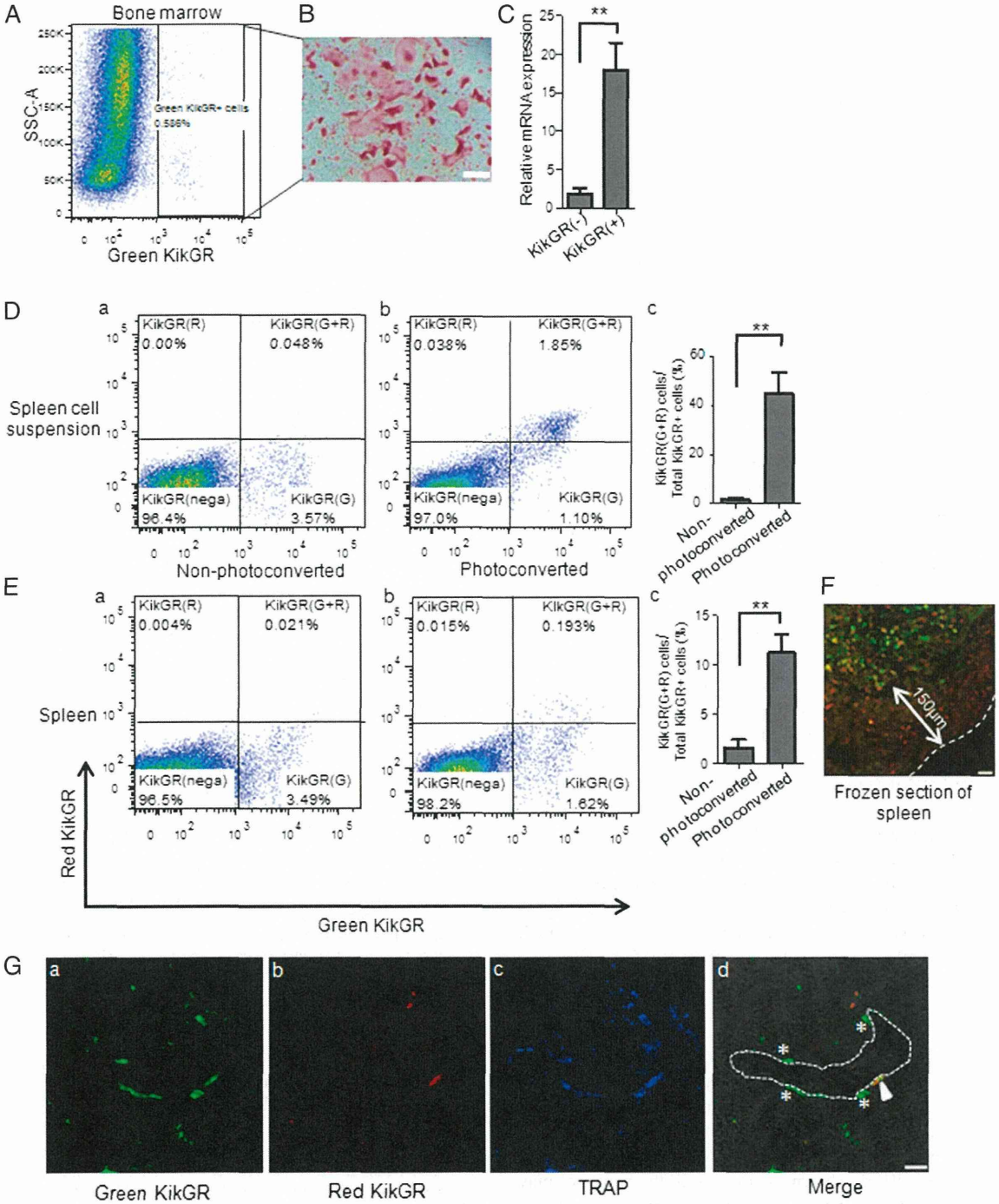

FIGURE 4. Tracking the circulation of osteoclast precursors in KikGR transgenic mice in vivo. (**A**) Separation of the KikGR$^+$ cell population by flow cytometry. (**B**) Representative images of TRAP$^+$ osteoclast-like cells generated from KikGR$^+$ cells cultured with M-CSF (10 ng/ml) and RANKL (50 ng/ml). Scale bar, 200 μm. (**C**) Real-time quantitative PCR analysis of mRNA for Rank expression in KikGR$^+$ cells and KikGR$^-$ cells. Data represent the mean ± SEM (n = 3). (**D**) Flow cytometric analysis of non-photoconverted (**a**) and photoconverted (**b**) spleen cells. (**E**) Spleens were exposed as described in the *Materials and Methods* section, and wounds were closed surgically on day 0 (**b**). Non-photoconverted spleen cells are shown as a control (**a**). (D and E) The corresponding proportions of red KikGR$^+$ cells are shown (**c**). Data represent the mean ± SEM Three animals were independently analyzed. (**F**) Frozen spleen sections were visualized by confocal microscopy immediately after violet light irradiation. Scale bar, 30 μm. (**G**) Femoral bone tissues. Fluorescence image of green KikGR (**a**), fluorescence image of red KikGR (**b**), staining for TRAP (**c**), and overlay with a transmission image (**d**). Arrowhead, green and red mature KikGR$^+$ osteoclast; asterisks, green mature KikGR$^+$ osteoclasts. Scale bar, 30 μm. $^{**}p < 0.01$ (two-tailed unpaired t test).

ficiency in the spleen after exposure to violet light in situ. Spleens were accessed by making small incisions in the skin and were exposed to violet light (436 nm). A total of 11.28 ± 1.90% (mean ± SEM; n = 3) of KikGR in these cells was photoconverted and showed shifts in emission spectra (Fig. 4E). Histological examination of spleens showed that only KikGR-expressing cells near the surface of the spleen could be photoconverted (Fig. 4F), which explains the low efficiency compared with single-cell suspension.

Under bone-resorptive conditions induced by the application of RANKL, we detected a small number of mature TRAP$^+$ osteoclasts

that expressed red (photoconverted) KikGR (Fig. 4G). This result clearly demonstrates that osteoclast precursors from the spleen migrated to the bone marrow and differentiated into mature osteoclasts during these 2 d.

Discussion

Using two different experimental methods, we clearly demonstrated that circulating monocytoid precursors are capable of differentiating into osteoclasts, although we think that osteoclasts can also be derived from precursors within the same bone marrow cavity. We showed that some osteoclast precursors exit the bone marrow after they have been produced by hematopoiesis, circulate via the bloodstream, and enter the bone spaces that need to be resorbed. What is the relevance of this detour for osteoclast formation? Bone resorption does not occur homogeneously in all bone tissues (32). This implies that the site of bone resorption is not necessarily the same as that of osteoclast precursor generation. The most extreme example is bone destruction in arthritic joints, such as in fingers, where hematopoiesis is not so dominant. The versatile circulation system of monocytoid precursors would be reasonable and beneficial for delivering osteoclast precursors from their site of origin to the site that actually needs bone destruction (33). More importantly, we showed that the recruitment of circulating precursor monocytes into the bone marrow cavity was enhanced by bone-resorptive states, such as that induced by RANKL treatment. These results suggest that unknown mechanisms control precursor recruitment in a RANKL-dependent manner. In this regard, we have to be aware that parabiotic mice were under conditions of slightly increased bone resorption because of their restricted motion, as observed in the tail suspension model (34). Fewer circulating precursor monocytes may be recruited under more physiological (nonparabiotic) conditions (Supplemental Fig. 2).

The system presented shows marked differences from the development of other monocytoid cells such as microglia, which are essentially derived from primordial tissue-resident precursors (11). We also found that no $EGFP^+$ microglia could be detected in the brain of the wild-type mice of the parabiotic pairs, whereas small numbers of dermal dendritic cells and liver Kupffer cells were $EGFP^+$ (data not shown). These results suggest that different types of monocytoid cells have intrinsic modes of precursor cell recruitment in situ.

The molecular mechanisms of egress and entry of circulating osteoclast precursors from and to the bone marrow remain to be elucidated. Several chemokines and lipid mediators, including SDF-1/CXCL12 and S1P, have been reported to be involved in osteoclast precursor localization (6, 7). Now that osteoclast precursors have been clearly shown to circulate in the body, we may consider a novel line of therapy for bone-resorptive diseases that targets the migratory behavior of osteoclast precursors. Most anti–bone resorption drugs, including bisphosphonates, target mature osteoclasts (35). The new therapeutic approach proposed in this study has completely different pharmacological properties and may be promising for future drug discoveries in this field.

Acknowledgments

We thank Dr. Satoshi Ueha (The University of Tokyo) for helpful discussion regarding the analyses on the mobilization of circulating monocytes. We also thank Mai Shirazaki and Masami Kasaoka (Osaka University) for technical assistance.

Disclosures

The authors have no financial conflicts of interest.

References

1. Teitelbaum, S. L., and F. P. Ross. 2003. Genetic regulation of osteoclast development and function. *Nat. Rev. Genet.* 4: 638–649.
2. Xing, L., E. M. Schwarz, and B. F. Boyce. 2005. Osteoclast precursors, RANKL/RANK, and immunology. *Immunol. Rev.* 208: 19–29.
3. Yao, Z., P. Li, Q. Zhang, E. M. Schwarz, P. Keng, A. Arbini, B. F. Boyce, and L. Xing. 2006. Tumor necrosis factor-alpha increases circulating osteoclast precursor numbers by promoting their proliferation and differentiation in the bone marrow through up-regulation of c-Fms expression. *J. Biol. Chem.* 281: 11846–11855.
4. Mizoguchi, T., A. Muto, N. Udagawa, A. Arai, T. Yamashita, A. Hosoya, T. Ninomiya, H. Nakamura, Y. Yamamoto, S. Kinugawa, et al. 2009. Identification of cell cycle-arrested quiescent osteoclast precursors in vivo. *J. Cell Biol.* 184: 541–554.
5. Muto, A., T. Mizoguchi, N. Udagawa, S. Ito, I. Kawahara, Y. Abiko, A. Arai, S. Harada, Y. Kobayashi, Y. Nakamichi, et al. 2011. Lineage-committed osteoclast precursors circulate in blood and settle down into bone. *J. Bone Miner. Res.* 26: 2978–2990.
6. Ishii, T., Y. Shimazu, I. Nishiyama, J. Kikuta, and M. Ishii. 2011. The role of sphingosine 1-phosphate in migration of osteoclast precursors; an application of intravital two-photon microscopy. *Mol. Cells* 31: 399–403.
7. Kollet, O., A. Dar, S. Shivtiel, A. Kalinkovich, K. Lapid, Y. Sztainberg, M. Tesio, R. M. Samstein, P. Goichberg, A. Spiegel, et al. 2006. Osteoclasts degrade endosteal components and promote mobilization of hematopoietic progenitor cells. *Nat. Med.* 12: 657–664.
8. Cambier, J. C., S. B. Gauld, K. T. Merrell, and B. J. Vilen. 2007. B-cell anergy: from transgenic models to naturally occurring anergic B cells? *Nat. Rev. Immunol.* 7: 633–643.
9. Berg, L. J. 2007. Signalling through TEC kinases regulates conventional versus innate CD8(+) T-cell development. *Nat. Rev. Immunol.* 7: 479–485.
10. Merad, M., M. G. Manz, H. Karsunky, A. Wagers, W. Peters, I. Charo, I. L. Weissman, J. G. Cyster, and E. G. Engleman. 2002. Langerhans cells renew in the skin throughout life under steady-state conditions. *Nat. Immunol.* 3: 1135–1141.
11. Ginhoux, F., M. Greter, M. Leboeuf, S. Nandi, P. See, S. Gokhan, M. F. Mehler, S. J. Conway, L. G. Ng, E. R. Stanley, et al. 2010. Fate mapping analysis reveals that adult microglia derive from primitive macrophages. *Science* 330: 841–845.
12. Flügel, A., M. Bradl, G. W. Kreutzberg, and M. B. Graeber. 2001. Transformation of donor-derived bone marrow precursors into host microglia during autoimmune CNS inflammation and during the retrograde response to axotomy. *J. Neurosci. Res.* 66: 74–82.
13. Nagasawa, T. 2006. Microenvironmental niches in the bone marrow required for B-cell development. *Nat. Rev. Immunol.* 6: 107–116.
14. Ishii, M., J. G. Egen, F. Klauschen, M. Meier-Schellersheim, Y. Saeki, J. Vacher, R. L. Proia, and R. N. Germain. 2009. Sphingosine-1-phosphate mobilizes osteoclast precursors and regulates bone homeostasis. *Nature* 458: 524–528.
15. Ishii, M., J. Kikuta, Y. Shimazu, M. Meier-Schellersheim, and R. N. Germain. 2010. Chemorepulsion by blood S1P regulates osteoclast precursor mobilization and bone remodeling in vivo. *J. Exp. Med.* 207: 2793–2798.
16. Boban, I., C. Jacquin, K. Prior, T. Barisic-Dujmovic, P. Maye, S. H. Clark, and H. L. Aguila. 2006. The 3.6 kb DNA fragment from the rat Col1a1 gene promoter drives the expression of genes in both osteoblast and osteoclast lineage cells. *Bone* 39: 1302–1312.
17. Boban, I., T. Barisic-Dujmovic, and S. H. Clark. 2010. Parabiosis model does not show presence of circulating osteoprogenitor cells. *Genesis* 48: 171–182.
18. Harris, R. B. 1999. Parabiosis between db/db and ob/ob or db/+ mice. *Endocrinology* 140: 138–145.
19. Tsutsui, H., S. Karasawa, H. Shimizu, N. Nukina, and A. Miyawaki. 2005. Semi-rational engineering of a coral fluorescent protein into an efficient highlighter. *EMBO Rep.* 6: 233–238.
20. Tomura, M., N. Yoshida, J. Tanaka, S. Karasawa, Y. Miwa, A. Miyawaki, and O. Kanagawa. 2008. Monitoring cellular movement in vivo with photoconvertible fluorescence protein "Kaede" transgenic mice. *Proc. Natl. Acad. Sci. USA* 105: 10871–10876.
21. Tomura, M., T. Honda, H. Tanizaki, A. Otsuka, G. Egawa, Y. Tokura, H. Waldmann, S. Hori, J. G. Cyster, T. Watanabe, et al. 2010. Activated regulatory T cells are the major T cell type emigrating from the skin during a cutaneous immune response in mice. *J. Clin. Invest.* 120: 883–893.
22. Tomura, M., K. Itoh, and O. Kanagawa. 2010. Naive CD4+ T lymphocytes circulate through lymphoid organs to interact with endogenous antigens and upregulate their function. *J. Immunol.* 184: 4646–4653.
23. Jung, S., J. Aliberti, P. Graemmel, M. J. Sunshine, G. W. Kreutzberg, A. Sher, and D. R. Littman. 2000. Analysis of fractalkine receptor CX(3)CR1 function by targeted deletion and green fluorescent protein reporter gene insertion. *Mol. Cell. Biol.* 20: 4106–4114.
24. Maeda, K., Y. Kobayashi, N. Udagawa, S. Uehara, A. Ishihara, T. Mizoguchi, Y. Kikuchi, I. Takada, S. Kato, S. Kani, et al. 2012. Wnt5a-Ror2 signaling between osteoblast-lineage cells and osteoclast precursors enhances osteoclastogenesis. *Nat. Med.* 18: 405–412.
25. Jiang, Q., R. Oldenburg, S. Otsuru, A. E. Grand-Pierre, E. M. Horwitz, and J. Uitto. 2010. Parabiotic heterogenetic pairing of $Abcc6^{-/-}$/$Rag1^{-/-}$ mice and their wild-type counterparts halts ectopic mineralization in a murine model of pseudoxanthoma elasticum. *Am. J. Pathol.* 176: 1855–1862.
26. Kawamoto, T. 2003. Use of a new adhesive film for the preparation of multi-purpose fresh-frozen sections from hard tissues, whole-animals, insects and plants. *Arch. Histol. Cytol.* 66: 123–143.
27. Klauschen, F., M. Ishii, H. Qi, M. Bajénoff, J. G. Egen, R. N. Germain, and M. Meier-Schellersheim. 2009. Quantifying cellular interaction dynamics in 3D fluorescence microscopy data. *Nat. Protoc.* 4: 1305–1311.

28. Parfitt, A. M., M. K. Drezner, F. H. Glorieux, J. A. Kanis, H. Malluche, P. J. Meunier, S. M. Ott, and R. R. Recker; Report of the ASBMR Histomorphometry Nomenclature Committee. 1987. Bone histomorphometry: standardization of nomenclature, symbols, and units. *J. Bone Miner. Res.* 2: 595–610.
29. Koizumi, K., Y. Saitoh, T. Minami, N. Takeno, K. Tsuneyama, T. Miyahara, T. Nakayama, H. Sakurai, Y. Takano, M. Nishimura, et al. 2009. Role of CX3CL1/fractalkine in osteoclast differentiation and bone resorption. *J. Immunol.* 183: 7825–7831.
30. Tomimori, Y., K. Mori, M. Koide, Y. Nakamichi, T. Ninomiya, N. Udagawa, and H. Yasuda. 2009. Evaluation of pharmaceuticals with a novel 50-hour animal model of bone loss. *J. Bone Miner. Res.* 24: 1194–1205.
31. Nakagawa, N., M. Kinosaki, K. Yamaguchi, N. Shima, H. Yasuda, K. Yano, T. Morinaga, and K. Higashio. 1998. RANK is the essential signaling receptor for osteoclast differentiation factor in osteoclastogenesis. *Biochem. Biophys. Res. Commun.* 253: 395–400.
32. Aguirre, J. I., L. I. Plotkin, S. A. Stewart, R. S. Weinstein, A. M. Parfitt, S. C. Manolagas, and T. Bellido. 2006. Osteocyte apoptosis is induced by weightlessness in mice and precedes osteoclast recruitment and bone loss. *J. Bone Miner. Res.* 21: 605–615.
33. Danks, L., A. Sabokbar, R. Gundle, and N. A. Athanasou. 2002. Synovial macrophage-osteoclast differentiation in inflammatory arthritis. *Ann. Rheum. Dis.* 61: 916–921.
34. Amblard, D., M. H. Lafage-Proust, A. Laib, T. Thomas, P. Rüegsegger, C. Alexandre, and L. Vico. 2003. Tail suspension induces bone loss in skeletally mature mice in the C57BL/6J strain but not in the C3H/HeJ strain. *J. Bone Miner. Res.* 18: 561–569.
35. Reszka, A. A., and G. A. Rodan. 2003. Mechanism of action of bisphosphonates. *Curr. Osteoporos. Rep.* 1: 45–52.

Gene Therapy (2012) 19, 561–569

www.nature.com/gt

ORIGINAL ARTICLE

Early intra-amniotic gene transfer using lentiviral vector improves skin blistering phenotype in a murine model of Herlitz junctional epidermolysis bullosa

M Endo[1], PW Zoltick[1], A Radu[1], J Qiujie[2], C Matsui[3], PM Marinkovich[4], J McGrath[5], K Tamai[6], J Uitto[2] and AW Flake[1]

Mutations of the *LAMB3* gene cause a lethal form of junctional epidermolysis bullosa (JEB). We hypothesized that early intra-amniotic gene transfer in a severe murine model of JEB would improve or correct the skin phenotype. Time-dated fetuses from heterozygous LAMB3^{IAP} breeding pairs underwent ultrasound guided intra-amniotic injection of lentiviral vector encoding the murine *LAMB3* gene at embryonic day 8 (E8). Gene expression was monitored by immunohistochemistry. The transgenic laminin-β3 chain was shown to assemble with its endogenous partner chains, resulting in detectable amounts of laminin-332 in the basement membrane zone of skin and mucosa. Ultrastructually, the restoration of ~60% of hemidesmosomal structures was also noted. Although we could correct the skin phenotype in 11.9% of homozygous LAMB3^{IAP} mice, none survived beyond 48 h. However, skin transplants from treated E18 homozygous LAMB3^{IAP} fetuses maintained normal appearance for 6 months with persistence of normal assembly of laminin-332. These results demonstrate for the first time long-term phenotypic correction of the skin pathology in a severe model of JEB by *in vivo* prenatal gene transfer. Although survival remained limited due to the limitations of this mouse model, this study supports the potential for treatment of JEB by prenatal gene transfer.
Gene Therapy (2012) **19**, 561–569; doi:10.1038/gt.2011.135; published online 22 September 2011

Keywords: prenatal gene therapy; lentiviral vector; epidermolysis bullosa

INTRODUCTION

Epidermolysis bullosa (EB) is a group of heritable blistering disorders caused by mutations in genes expressed in the cutaneous basement membrane zone (BMZ) that cause considerable morbidity and mortality. Recently, several molecular therapies are being investigated for the treatment of patients with different subtypes of EB, including *ex vivo* gene therapy,[1] protein replacement[2] and cellular therapy.[3–7] Herlitz junctional epidermolysis bullosa (HJEB) is one of the most severe variants of EB characterized by extensive mucocutaneous blistering and erosions at birth leading to early lethality.[8,9] HJEB, an autosomal recessive disease, is caused by mutations in any of the genes encoding the subunit polypeptides laminin-α3, laminin-β3 or laminin-χ2 of the heterotrimeric laminin-332 protein. Currently, there is no specific cure or effective treatment for HJEB. Based on the early onset of severe blister formation, HJEB is a compelling candidate for *in vivo* prenatal gene therapy.

Potential advantages of prenatal gene therapy include the small size of the fetus, high frequency and accessibility of stem cell populations, and fetal immunologic immaturity that may facilitate tolerance for transgene encoded novel proteins.[10,11] The skin is potentially an ideal target for gene correction *in utero*. Because the fetus is surrounded with amniotic fluid, the entire fetal skin surface can theoretically be exposed to a vector with a single injection into the amniotic cavity. Although the majority of efforts to transduce skin by the intra-amniotic route have achieved efficient gene expression, the duration of expression has been limited to 3–4 weeks, corresponding to the time required for a complete epidermal turnover cycle consistent with failure to transduce the skin stem cell population.[12–17]

Effective gene therapy for skin disorders will require gene transfer to the skin stem cell populations to achieve long-term expression due to rapid cellular turnover inherent to the epidermis. There have been two types of stem cells identified in the epidermis: the basal cell and the bulge stem cell.[18–22] Unfortunately, once the skin becomes stratified through epidermal differentiation, these stem cell populations are no longer accessible via the amniotic fluid. However, there is a stage during early embryonic development when the skin is comprised of only a single layer and all nascent skin stem cell populations are exposed to the amniotic fluid.[23] Based on this opportunity, in our previous study we injected lentiviral vector encoding the murine *LAMB3* gene under control of the human keratin 5 promoter into the amniotic cavity at embryonic day 8 or 9 (E8/9) of gestation in mouse embryos. We demonstrated efficient transfer of reporter gene to the skin stem cell populations with subsequent life-long expression of the transgene.[24]

[1]Department of Surgery, The Children's Center for Fetal Research, The Children's Hospital of Philadelphia, University of Pennsylvania School of Medicine, Abramson Research Center, Philadelphia, PA, USA; [2]Department of Dermatology and Cutaneous Biology, Thomas Jefferson University, Philadelphia, PA, USA; [3]Department of Dermatology, University of Toyama, Toyama, Japan; [4]Department of Medical Dermatology, Stanford University, Redwood City, CA, USA; [5]Division of Genetics and Molecular Medicine, Genetic Skin Disease Group, St John's Institute of Dermatology, The Guy's, King's College, and St Thomas' School of Medicine, London, UK and [6]Division of Gene Therapy Science, Osaka University Graduate School of Medicine, Osaka, Japan

Correspondence: Dr AW Flake, Department of Surgery, The Children's Center for Fetal Research, The Children's Hospital of Philadelphia, University of Pennsylvania School of Medicine, Abramson Research Center, Room 1116B, 3615 Civic Center Boulevard, Philadelphia, PA 19104-4318, USA.
E-mail: flake@email.chop.edu
Received 13 June 2011; revised 2 August 2011; accepted 8 August 2011; published online 22 September 2011

In this study, we have applied the early gestational intra-amniotic gene transfer (IAGT) method to the murine model of HJEB, the homozygous LAMB3^{IAP} mouse, which completely lacks laminin-332 manifest by severe perinatal blistering and demise in the perinatal period.[25] Our results demonstrate for the first time long-term phenotypic correction of the skin pathology in a model of severe JEB by *in vivo* prenatal gene transfer. Although survival remained limited due to the limitations of this mouse model, this study supports the potential for clinical treatment of JEB by prenatal gene transfer.

RESULTS

Viability of fetuses following IAGT

A total of 566 fetal mice from 68 pregnant females derived from heterozygous LAMB3^{IAP} timed matings were injected with lentiviral vector encoding laminin-β3 on embryonic day 8 (E8). We used an ultrasound guided injection system to visualize and inject into the amniotic space as previously described.[26,27]

To detect any improvement in survival of homozygous EB mice after IAGT, we analyzed a subset of 162 injected mice from 20 of the 68 pregnant females 48 h after birth (P2). Their survival rate was 24.7% (40/162) and genotyping of these mice revealed that 65.0% of these (26/40) were heterozygous and 35.0% (14/40) were wild type (WT). There were no surviving homozygous LAMB3^{IAP} mice in this group, demonstrating that we had not improved survival in this model by IAGT beyond 48 h. To further assess the results of IAGT, and avoid the variables involved in neonatal survival in this mouse model, we decided to harvest the injected mice before birth. The subsequent 408 fetuses from 48 of the 68 pregnant females were analyzed before birth (on E18, 19 or 20). The total survival rate until harvest was 55.2% (223/408) and genotyping of these mice revealed that 50.2% (112/223) were heterozygous, 30.9% (69/223) were WT and 18.8% (42/223) were homozygous (Table 1).

Restoration of laminin-β3 and laminin-332 expression

To determine whether the *LAMB3* gene was expressed in the BMZ of the treated homozygous LAMB3^{IAP} mice, we performed immunofluorescent staining with monoclonal anti-laminin-β3 antibody on skin harvested at E18/19/20. As expected, untreated homozygous LAMB3^{IAP} mice showed no immunoreactivity to anti-laminin-β3 antibody (Figure 1a). However, homozygous LAMB3^{IAP} mice after treatment by E8 IAGT expressed laminin-β3 at the basement membrane in a linear pattern (Figure 1e).

Since the *LAMB3* gene encodes one subunit of the heterotrimeric laminin-332 molecule, restoration of synthesis of the β3 subunit should restore assembly of functional laminin-332 molecules. To assess the restoration of the laminin-332 complex, we performed immunofluorescent staining with polyclonal anti-laminin-332 antibody on skin sections of E8 IAGT treated homozygous LAMB3^{IAP} mice harvested at E18/19/20. Treated homozygous LAMB3^{IAP} mice demonstrated expression of laminin-332 at the basement membrane in a linear pattern (Figure 1f).

Table 1 Genotype and phenotype of mice undergoing E8 IAGT

Total E8 IAGT dam (N=68)	*Analyzed 48 h after birth* (N=20)	*Analyzed before birth* (N=48)
E8 intra-amniotic injection		
Pregnant pups	162	408
Injected pups	162 (100)	404 (99.0)
Survival pups	40 (24.7)	223 (55.2)
Genotype of survival pups	Total=40	Total=223
WT	14 (35)	69 (30.9)
Hetero	26 (65)	112 (50.2)
Null	0 (0)	42 (18.8)
Phenotype of null pups		Total=42
Null phenotype		37 (88.1)
WT phenotype		5 (11.9) $P<0.005$[a]

Abbreviations: IAGT, intra-amniotic gene transfer; WT, wild type.
[a]*P*-value for skin phenotype comparison between E8 IAGT treated null pups (n=42) and non-treated null pups (n=89) by using the Fisher's exact test.

Assessments of restoration of skin phenotype

To determine whether expression of the *LAMB3* transgene and concomitant restoration of laminin-332 could rescue the skin phenotype, we performed phenotypic assessment by the mechanical skin disruption test (pinch test). In untreated homozygous LAMB3^{IAP} mice, when we performed the pinch test, all null mice failed the test at the first attempt (n=89). We harvested a total of 223 E8 IAGT mice by cesarean section at E18/19/20. No fetal mice demonstrated evidence of skin blistering at delivery. We performed the pinch test and found that in 37 out of 223 fetal mice the skin was disrupted. On subsequent genotyping, 42 homozygous mice were identified. Of the 42 genotypically homozygous mice treated by E8 IAGT, five (11.9%) mice demonstrated phenotypic correction by this relatively rigorous test (Table 1). None of the genotypically WT or heterozygous mice had a positive pinch test. Statistical analyses (Fisher's exact test) confirmed that E8 IAGT homozygous LAMB3^{IAP} mice significantly restored the skin phenotype compared with untreated LAMB3^{IAP} homozygous mice (Table 1). To assess why the majority of treated null mice failed the pinch test, we performed immunofluorescent staining for laminin-β3 and laminin-332 at the site of mechanical disruption. Despite the presence of mechanical disruption, we were able to detect laminin-β3 and laminin-332 expression at the BMZ within the lesions (Figure 2). We also assessed viral copy number by qPCR analysis in skin between two null mice that failed and two null mice that passed the pinch test but found no correlation between copy number and phenotypic restoration (data not shown).

Restoration of hemidesmosomal structures by E8 IAGT

Based on the original description, the homozygous LAMB3^{IAP} mouse is characterized by the formation of abnormal hemidesmosomal structures.[25] The hemidesmosomes appear less distinct and inner and outer plaques more diffuse than in WT mice, and the sub-basal dense plate (SBDP) is completely absent. To determine whether the restoration of laminin-β3 could correct the defect in hemidesmosome formation at the BMZ, electron microscopy was performed at E19 on skin sections of E8 IAGT treated homozygous LAMB3^{IAP} mice, untreated homozygous LAMB3^{IAP} mice (negative control) and WT mice (positive control). As shown in Figure 3a, E8 IAGT of *LAMB3* transgene could restore normal hemidesmosomal structures, thus demonstrating correction of the major ultrastructual abnormality seen in HJEB skin.

To quantitatively assess the efficiency of restoration of hemidesmosomal structures, we compared the percentages of normal hemidesmosomes in an E8 IAGT homozygous LAMB3^{IAP} mouse with an untreated homozygous LAMB3^{IAP} mouse, and a WT mouse. For this purpose, we counted the presence of the SBDP as the critical feature of normal hemidesmosome structure. There are two reasons to choose

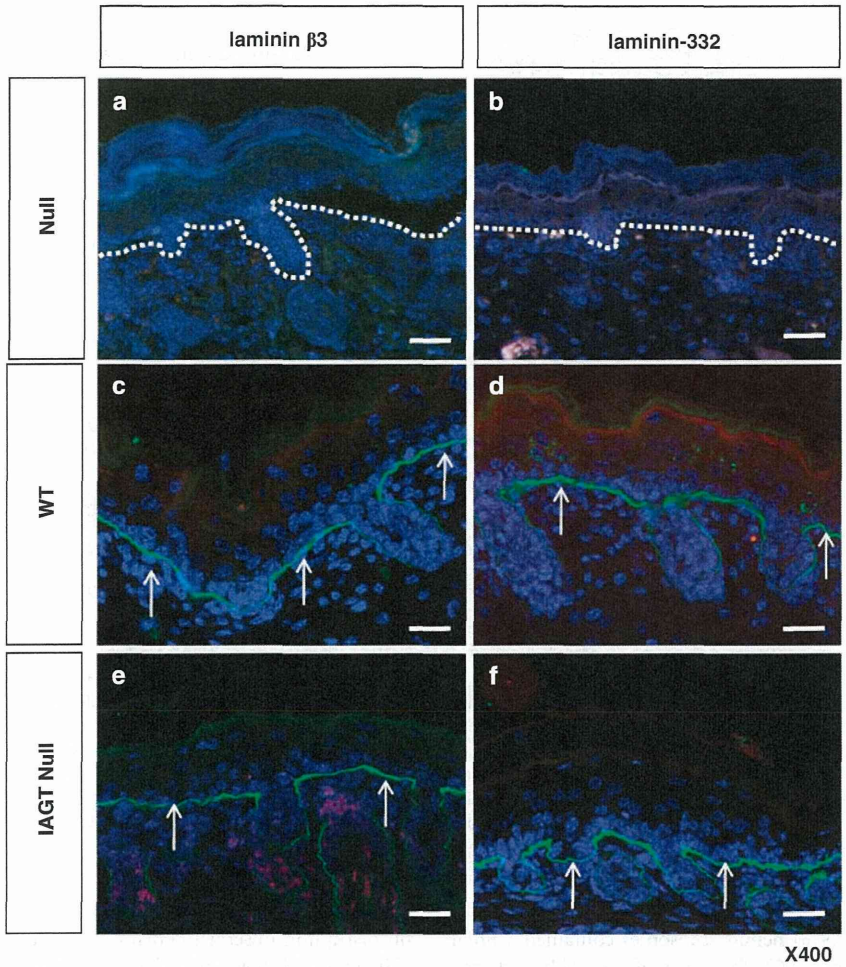

Figure 1 Immunofluorescence analysis of skin samples from untreated homozygous LAMB3^{IAP} mice (defined as 'null') (**a**, **b**), WT mice (defined as 'WT') (**c**, **d**) and homozygous LAMB3^{IAP} mice treated by E8 IAGT with lentiviral-*LAMB3* (defined as 'IAGT null') (**e**, **f**). No expression of either laminin-β3 or laminin-332 is seen in the BMZ in untreated null mice. The white dotted lines indicate the position of the basal lamina. (**a**, **b**) WT mice are positive for laminin-β3 and laminin-332 staining in a linear pattern along the basement membrane. (**c**, **d**) Treated null mice stain positive for laminin-β3 and laminin-332 at the basement membrane in a similar pattern to WT mice arrows (arrows, **e**, **f**). The sections were counterstained with 4',6-diamidino-2-phenylindole to visualize the cells (blue) (scale bar=100 μm).

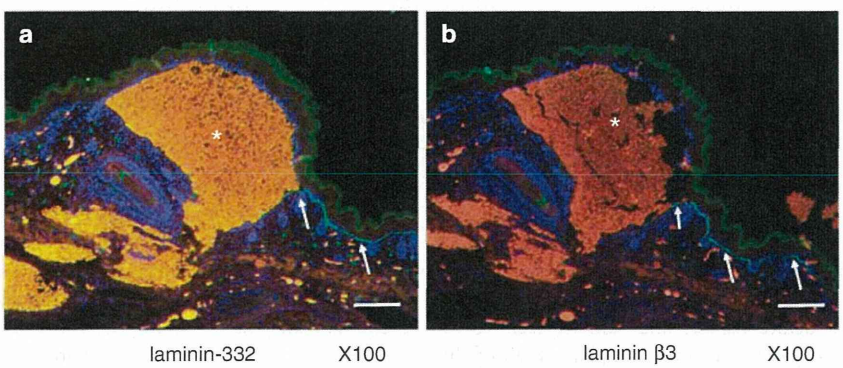

Figure 2 Immunofluorescence analysis of blistered skin samples from E8 IAGT null mice. Both laminin-β3 (**a**) and laminin-332 (**b**) were expressed as a linear pattern (arrows) in the BMZ surrounding the blistered area with contained hemorrhage (*) (scale bar=25 μm).

the SBDP as a landmark: (1) the SBDP is theoretically absent in null mice and (2) the SBDP is comparatively easy to detect regardless of various sectioning plane. In WT mice, 58 out of 81 (71.6%) hemidesmosomes had a detectable SBDP. In contrast, only 10 out of 92 (10.9%) hemidesmosomes in the untreated homozygous LAMB3^{IAP} mouse contained a SBDP. In the treated homozygous LAMB3^{IAP}

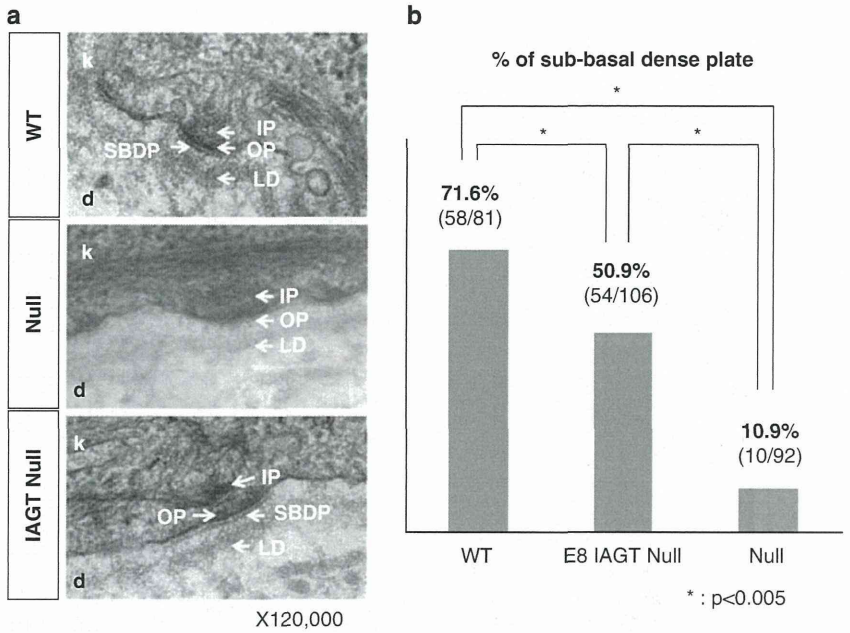

Figure 3 Transmission electron microscopy of dermo-epidermal junction. (**a**) Electron micrographs of skin sections demonstrate the junction between the basal keratinocytes (k) of the epidermis and the upper reticular dermis (d). In the WT mice, the hemidesmosomes are visible at the basal surface of the keratinocytes and are comprised of an inner plaque (IP), outer plaque (OP) and SBDP. The BMZ, consisting of the electron-opaque lamina lucida and the electron-dense lamina densa, runs parallel to the keratinocyte basal membrane. In homozygous LAMB3^{IAP} mice (null), the hemidesmosomes are present but appear less distinct and the inner and OPs are more diffuse than in the WT mice, and the SBDP is absent. In homozygous LAMB3^{IAP} mice treated by E8 IAGT with lentiviral-*LAMB3* (IAGT null), the normal structures of the desmosomes are restored. (**b**) Bar graph demonstrating the percentage of hemidesmosomes (HD) with a demonstrable SBDP. A blinded examiner with expertise in skin electron microscopy counted the number of the HD and determined the presence or absence of the SBDP. **P*-values <0.005 for positive SBDP comparison between WT, E8 IAGT null and non-treated null pups by using the Fisher's exact test.

mouse, 54 out of 106 (50.9%) hemidesmosomes contained a SBDP. If we normalize the data to a 100% frequency of normal hemidesmosomes in WT and 0% in LAMB3^{IAP} homozygous mice, the hemidesmosome restoration rate in E8 IAGT homozygous LAMB3^{IAP} mice was 65.9% (restoration rate=(50.9–10.9)×100/(71.6–10.9)%). Statistical analyses (Fisher's exact test) confirmed that E8 IAGT homozygous LAMB3^{IAP} mice significantly restored the hemidesmosomal structures compared with untreated LAMB3^{IAP} homozygous mice (Figure 3b).

Skin graft assessment

As we were unable to improve survival in this murine model by IAGT, we elected to assess long-term correction of the skin phenotype in a skin transplant model. The donor skins were harvested from E8 IAGT homozygous LAMB3^{IAP} fetuses (the LAMB3^{IAP} mice are on a B6 background) at E18 and they were grafted onto 6- to 8-week-old, female B6-*GFP* transgenic mice. We used *GFP* transgenic mice to allow easy recognition of the grafted skin, and allow identification of any recipient-derived cells in the skin grafts. The donor skin was harvested from treated homozygous LAMB3^{IAP} mice that were assessed by the pinch test before harvest and skin transfer. To be sure that only treated homozygous skin was transplanted, all of the grafted donor skin came from mice that failed the mechanical disruption test. A total of five donor skin samples from five mice were transplanted and four of the five successfully engrafted (80%). The skin grafts on the recipients maintained a normal appearance for 6 months at which time the experiment was terminated. We assessed the grafted skin by the pinch test after a skin graft was established with no disruption observed and no visible subsequent blister formation. Skin grafts of age-matched untreated homozygous LAMB3^{IAP} fetal mice (N=14) uniformly failed to engraft within 2 weeks after transplantation (0%). As our technical control, age-matched B6 fetal skin was transplanted onto *GFP* transgenic mice (N=5) and 5 of 5 grafts were successful (100%) (Figure 4A). We confirmed the persistence of the skin grafts by fluorescence stereomicroscopy, which demonstrated GFP-negative skin grafts, surrounded by GFP-positive recipient skin (Figure 4B). Immunohistology of the skin grafts demonstrated *LAMB3* transgene expression with normal laminin-β3 chain assembly as evidenced by laminin-332, in the BMZ. As expected, there were many GFP-positive cells in the dermis, but we could not detect any GFP-positive keratinocytes in the skin grafts (Figure 5).

DISCUSSION

In this study, we used an HJEB mouse model (homozygous LAMB3^{IAP} mouse) to evaluate the feasibility of *in vivo* prenatal gene therapy for phenotypic correction of the skin pathology of a lethal junctional EB (HJEB). Our study demonstrated that E8 IAGT using lentiviral vector results in expression of laminin-β3 in the dermo-epidermal basement membrane and that the transgene encoded laminin-β3 can be incorporated in the assembly of the heterotrimeric laminin-332 protein. In addition, the laminin-332 can restore structurally normal hemidesmosomes in the BMZ of the HJEB mouse skin. The expression was detected in the skin as well as in the oral mucosa. In addition, we could demonstrate restoration of the skin phenotype by the mechanical disruption test in only 11% of treated homozygous animals. However, as the pinch test is a relatively rigorous, all or nothing assay

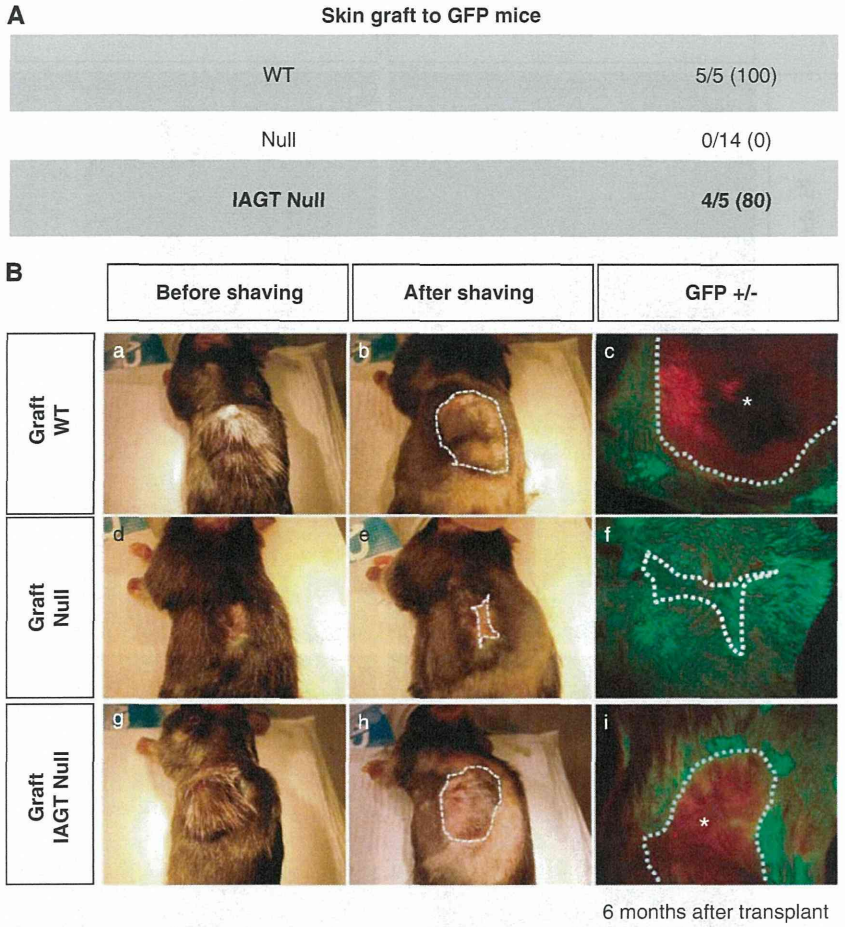

Figure 4 Prolonged skin graft survival after IAGT. The skin from homozygous LAMB3^{IAP} fetal mice treated by E8 IAGT with lentiviral-*LAMB3* (IAGT null) at E18 were grafted to the *GFP* Tg mice. Homozygous untreated LAMB3^{IAP} fetal mice were used as negative controls (null), and C57BL6 fetal mice as positive control (WT). (**A**) Table demonstrating successful engraftment rates in IAGT null, WT and null mice 6 months after skin grafting. (**B**) Macroscopic appearance of the grafted skin on *GFP* Tg mice with optical light (a, b, d, e, g, h) or fluorescent light (c, f, i) 6 months after graft surgery. Null skin graft (middle row) was completely lost and the skin defect was healed with host-derived skin. WT (top row) and E8 IAGT null skin grafts persisted without any obvious blistering or erosions.

that does not allow assessment of incremental improvement in phenotype, we decided to assess skin integrity in a model where long-term phenotypic correction could be monitored. In the skin transplant model, we were able to clearly demonstrate an improvement in phenotype with essentially equal skin graft survival and integrity in comparison to normal skin graft controls. In addition to the partial restoration of hemidesmosomes, there are at least two possible explanations for the neonatal failure of the pinch test and subsequent passage of the same test 6 months after transplantation. In adult skin, the additional mechanical support provided by the hair shafts to anchor the epidermis to the dermis, as well as simply the thickness of the skin in the adult versus the neonate may have provided adequate support to prevent shearing with the pinch test. Finally, despite the failure of the pinch test in neonatal skin, the ability of the corrected neonatal skin to engraft compared with complete loss of the non-treated skin supports a significant improvement skin integrity from the *in utero* treatment.

Despite improvement of the skin phenotype, we demonstrated no effect on survival of the newborn pups in this study. While this may be related to inadequate correction of the skin abnormality, other causes of death in this model may not have been addressed by IAGT and this may also be an issue with clinical application. Newborns with HJEB have major involvement of the airways, gastrointestinal and vesicourinary tracts and possibly abnormalities of T-cell development resulting in immune deficiency.[28] In the murine setting, this may have resulted in poor feeding, maternal neglect, hypoproteinemia, electrolyte abnormalities, sepsis and early demise. In the context of potential clinical application, it is important to emphasize that even full correction of the skin phenotype alone may not result in complete correction of manifestations of the disease.

Laminin-332 is one of the key molecules in the BMZ maintaining adhesion between the epidermis and dermis.[29] Although other BMZ molecules, such as collagen VII, can be produced not only by the keratinocytes but also by the fibroblasts,[30,31] laminin-332 is produced only by the keratinocytes at the basal layer in the epidermis,[32] and consequently, correction of the EB skin phenotype in HJEB requires transfer of the *LAMB3* gene to the basal layer of the epidermis. There have been several previous experimental studies of prenatal gene transfer to skin.[12–15,17] Because the embryonic skin is surrounded by amniotic fluid, the most common mode of gene transfer to the skin

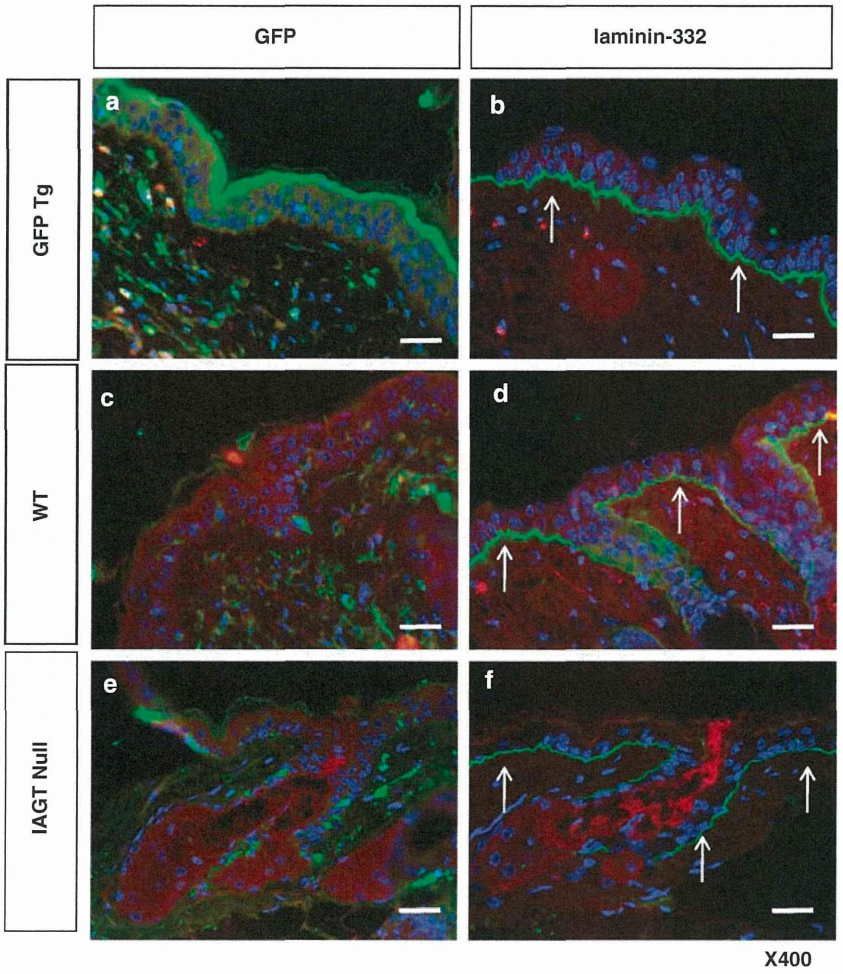

Figure 5 Immunofluorescent histologic appearance of skin grafts at 6 months after placement. (**a**, **b**) In the recipient skin, the epidermis is GFP positive and laminin-332 is seen in the BMZ in a linear pattern. (**c**, **d**) The WT grafted skin showed GFP-negative epidermis with expression of laminin-332. (**e**, **f**, arrows) In the IAGT null skin grafts, skin keratinocytes were GFP negative and expressed laminin-332 in the appropriate linear pattern at the BMZ (arrows). Some GFP-positive cells are seen in the dermis, but these are consistent with the infiltrate of cells derived from the host circulation with the same infiltration seen in WT donor grafts (scale bar=100 μm).

has been via IAGT. However, most previous studies have performed IAGT too late in development to achieve skin stem cell transduction, thus resulting in only transient gene expression. We have previously demonstrated that the window of opportunity for direct access to skin stem cell populations in the mouse is limited to the early gestational period from E8 to E9.[24] During that period, the skin exists as a single layer of cells, containing all of the nascent stem cells of the skin and skin appendages. Based on our previous marker gene study, we utilized the same approach to perform the IAGT at E8. We used a lentiviral vector construct expressing the *LAMB3* gene under control of the human keratin 5 promotor/enhancer (K5E), which was analogous to the GFP-encoding vector that demonstrated high efficiency transduction (~50%) of basal layer stem cells in our previous study.

Similar to our previous study, in this study we appear to have achieved efficient transduction of basal stem cells with long-term expression of the transgene encoded protein. In treated animals, we could demonstrate a linear pattern of expression of laminin-β3 and the assembly of laminin-332 heterotrimer in the cutaneous BMZ. As mentioned above, failure to improve survival in this murine model could be multifactorial and may or may not be reflective of failure to correct the skin phenotype. In addition to skin, HJEB affects the mucous membranes of the oropharynx, esophagus and the genitourinary tract.[33,34] While some expression of transgene is achieved in the oropharynx and tongue by E8 IAGT, the buccopharyngeal membrane is still intact and prevents access to stem cells in the posterior pharynx and esophagus.[35] Furthermore, the gene expression by E8 IAGT is mostly limited in the epidermal-derived organs.[35] This likely results in poor sucking and feeding by the pups with subsequent death from maternal neglect, cannibalism and/or dehydration. However, the relatively normal immunohistochemistry findings in combination with failure of the mechanical disruption test suggested that either the expression was quantitatively inadequate to fully correct the skin phenotype, or that the protein was being expressed but was functionally defective. The observation of associated restoration of laminin-332, confirmed expression of laminin-β3 in a form that can be incorporated into the trimer molecule, consistent with a functionally intact and appropriately expressed protein. We therefore tried to quantitatively assess the relative amount of laminin-332 in treated

mice versus untreated and normal mice by analysis of restoration of hemidesmosomes by electron microscopy. As hemidesmosomes are structural anchoring units in the BMZ, the degree of restoration of hemidesmosomes should roughly correspond to the degree of correction of skin integrity. Our analysis documented ~60% restoration of normal hemidesmosome structures in treated homozygous mice. As the mechanical disruption test is an all or nothing, extremely rigorous test of skin integrity, we wondered if we had accomplished a clinically significant degree of skin correction that would prevent skin blistering under normal circumstances of skin exposure. To directly test our treated skin under clinically relevant conditions of normal skin exposure, we performed skin transfer experiments to congenic *GFP* mice. The reason to use *GFP* transgenic mice is to allow easy recognition of the grafted skin, and allow identification of any recipient-derived cells in the skin grafts, which can potentially replace the native keratinocytes. On transfer of the treated skin grafts, despite harvest from mice that failed the mechanical disruption test, engrafted at a rate similar to control WT skin grafts and maintained their integrity without blister formation and with normal hair growth for 6 months. This was in marked contrast to grafts from untreated homozygous LAMB3^{IAP} mice, which were uniformly lost within 2 weeks.[36] The treated skin grafts showed no replacement by host keratinocytes, by either ingrowth or bone marrow derivation, supporting our conclusion that the expression of laminin-β3 in these grafts by E8 IAGT was quantitatively adequate to support normal skin function but inadequate to withstand the rigorous mechanical disruption test during the neonatal period in most circumstances. These results are supportive of the potential for prenatal gene correction in severe JEB, and perhaps in other forms of EB, and suggest that further improvements in the efficiency of IAGT could completely correct the skin phenotype. In addition, we have previously demonstrated that posterior pharyngeal and esophageal transduction can be achieved after resorption of the buccopharyngeal membrane (E9 in the mouse).[35] Therefore, from a clinical perspective, at least some of the extracutaneous manifestations of EB might also be correctable by this approach.

From a therapeutic perspective, this approach supports the promise of prenatal gene transfer for the treatment of genetic skin disorders such as EB in which defective protein synthesis occurs at the dermo-epidermal interface. However, there are a number of hurdles that would need to be overcome before any clinical application of this approach. First, although we have chosen to focus on skin gene transfer in this study, IAGT is not specific for skin.[26,35] While some selectivity occurs due to the limited interface between amniotic fluid and other fetal tissues, we have documented other tissues, including neuroectoderm,[35,37] that can be transduced by IAGT. This raises obvious concern about the potential for insertional mutagenesis, developmental effects and the potential for germ line alteration that exists for lentiviral vector-based approaches. These potential risks are, if anything, heightened by early gestational transduction. While greater tissue specificity and safety can probably be accomplished by the use of tissue-specific promoters or by regulated transgene expression, safer gene transfer techniques will need to be developed to alleviate these concerns. The second major impediment is that stage for stage, the timing of our early gestational injections between E8 and E11 in the mouse corresponds to the 21st to 55th day of gestation in human fetal development, a time in pregnancy that precedes current capabilities for prenatal diagnosis. Nevertheless, there has been rapid progress in prenatal diagnosis and in the foreseeable future, new approaches, such as genotyping of fetal cells or free fetal DNA in the maternal circulation, which can be found as early as the 5th week of gestation,[38] may allow for even earlier diagnosis of genetic disorders. Dilution of vector in the much larger volume of amniotic fluid in the human is a potential hurdle. However, the volume of human amniotic fluid at 7 weeks gestation is only 1.5 ml[39] (murine amniotic fluid volume at E8 is 350 nl) making the delivery of an equivalent concentration of lentiviral vector practically feasible. Finally, correction of skin phenotype alone will not cure the disease, and the prospect of partial treatment may not provide an acceptable quality of life for severely affected patients. However, we believe that with further optimization of this approach, alone or in combination with other therapies, prenatal gene transfer may ultimately have a role in the treatment of this devastating disease.

MATERIALS AND METHODS

Mice

Heterozygous LAMB3^{IAP} mice (obtained from Dr Pamela Swiatek, New York State Department of Health, Buffalo, NY, USA) and C57BL/6TgN actin-enhanced green fluorescent protein OsbY01 mice (obtained from Dr Okabe, Osaka University, Genome Information Research Center, Japan) were mated in our breeding colony. Heterozygous LAMB3^{IAP} matings were performed overnight and females were checked for vaginal plugs the next morning. The day of appearance of the vaginal plug was taken as E0. Pregnant females at E8 were utilized for IAGT. Animals were housed in the Laboratory Animal Facility of the Abramson Pediatric Research Center at The Children's Hospital of Philadelphia and were maintained in sterilized plastic microisolator cages and given sterilized standard laboratory chow and tap water *ad libitum*. Newborn mice were left with their mother and observed closely. All experimental protocols were reviewed and approved by the Institutional Animal Care and Use Committee at The Children's Hospital of Philadelphia, and followed guidelines set forth in the National Institutes of Health 'Guide for Care and Use of Laboratory Animals'. The genotype of the heterozygous/homozygous LAMB3^{IAP} animals was verified by PCR of the *LAMB3* gene and the IAP insertion with a template of genomic DNA from tail samples as previously described.[16]

Intra-amniotic cavity vector injection at E8

We used an ultrasound guided injection system (Vevo 660; VisualSonics, Toronto, Canada) for intra-amniotic vector injection of E8 pregnant mice. The anesthetic and surgical methods are as we have previously described.[26,27] A set volume of 350 nl of vector containing media was injected with an automated syringe.

Immunohistochemistry of laminin-β3/laminin-322

Tissue specimens collected for histology and immunohistochemistry were fixed in 10% buffered formalin solution (Sigma, St Louis, MO, USA) and embedded in paraffin. To evaluate and localize laminin-β3/laminin-322 protein in the harvested tissues, 4 μm sections were obtained using a paraffin microtome (Leica RM2035, Leica Instruments GmbH, Nussloch, Germany). Paraffin sections were incubated overnight at 53 °C and then deparaffinized in serial xylene washes, followed by rehydration through a graded alcohol series to deionized water. Enzymatic pre-treatment using proteinase K (Dako, Carpinteria, CA, USA) was applied to the sections for 10 min at RT (room temperature) followed by rinsing in deionized water and transferred to 0.1 M Tris-buffered saline pH 7.8. The tissue sections were incubated with the blocking solution (protein block serum free; Dako) for 10 min at RT. The blocking solutions were tapped off and the primary antibodies were applied overnight at 4 °C. Antibodies included polyclonal rabbit anti-laminin-332 (a gift from Dr Marinkovich, Stanford University, CA, USA) concentration of 1:400; Anti-laminin-β3[40] (a gift from Dr Matsui, Toyama University, Toyama, Japan) concentration of 1:50. On the following day, sections were washed for 10 min in Tris-buffered saline buffer at RT and Alexa Fluor 488 (Invitrogen, Carlsbad, CA, USA) was applied at 1:200 for 30 min at RT. Sections were then rinsed in Tris-buffered saline buffer and mounted with 4′,6-diamidino-2-phenylindole (Invitrogen) and analyzed using a Leica DMR microscope (Leica, Heerburg, Switzerland).

Transmission electron microscopic analysis

After euthanasia, skin samples were obtained from the arms of IAGT treated and untreated homozygous E18 LAMB3^{IAP} mice and of E19 C57BL6 mice, fixed in half strength Karnovsky's fixative, and embedded in epoxy resin. Ultrathin sections (80 nm) were stained sequentially with saturated uranyl acetate and Reynold's lead citrate.[41] Sections were imaged with a Jeol-1010 Transmission electron microscope (JEOL USA, Peabody, MA, USA).

Lentivector production containing the mouse LAMB3 or GFP under the human keratin 5 promoter/enhancer and cell culture

The human keratin 5 (K5) promoter, previously described,[24] was inserted into the HIV-1-based transfer vector, a modified F12 plasmid.[42] Inserted directly linked upstream of the promoter was the keratin 5 DNas I-hypersensitive site 4,[43] a strong keratinocyte-specific enhancer. The mouse *LAMB3* cDNA molecule, derived from total RNA extracted from keratinocytes using standard molecular protocols[44] with a coding sequence confirmed to be identical to that of GenBank Accession #NM_008484, was inserted into the lentivector transfer plasmid under the transcriptional control of the human keratin 5 promoter/enhancer (K5E). Alternatively, the GFP reporter was similarly inserted in the transfer plasmid replacing the therapeutic gene. Viral vectors, pseudotyped with the vesicular stomatitis virus-G protein envelope, were generated as previously reported using a three-plasmid transient cotransfection in HEK293-T cells. Viral supernatants were concentrated and, for the GFP vector, titered using serial dilutions as previously described and as determined on the mouse PAM212 and human HaCat T-cell lines (kind gifts from Dr George Cotsarelis, University of Pennsylvania). Titers of injected virus ranged from 1×10^9 and 3×10^{10} TU ml^{-1}. Virion production of the LAMB3 and also the GFP vectors were determined by measuring p24 by ELISA (ABL Inc., Kensington, MA, USA) according to the manufacturer's recommendations.

The PAM212 cells were grown in 1:3 Ham's F-12 medium (Gibco brand, Invitrogen Life Sciences, Carlsbad, CA, USA) and Dulbecco's modified Eagle's medium supplemented with 10% fetal calf serum and 1% penicillin/streptomycin. The HaCat T cells were cultured in Dulbecco's modified Eagle's medium with similar supplements.

Fluorescence microscopic analysis

We used fluorescent stereomicroscopy (MZ16FA; Leica) to distinguish between the donor and recipient skin in the skin transfer to *GFP* mouse experiments. For these studies, mice were euthanized 6 months after placement of the skin grafts and the skin was immediately dissected to allow direct visualization.

Mechanical skin disruption test (pinch test)

To assess the correction of skin phenotype, we performed the mechanical skin disruption or pinch test. The test is performed by pinching the murine skin between two fingers and performing a shearing motion to detach the epidermis. If the epidermis detached from the dermis, the test was recorded as a 'fail'. If the epidermis maintained its attachment, then it was recorded as a 'pass'. In animals that 'passed' the pinch test, we confirmed the result by using forceps to try to peel off the skin. If the epidermis detached from the dermis with the forceps, the mouse was recorded as a 'fail'. If the epidermis did not detach from the dermis, even when using the forceps, we classified the mouse as a 'WT phenotype'.

Skin grafting

Skin grafting was performed on 6- to 8-week-old, female GFP transgenic mice by a modification of the technique described by Billingham *et al.*[44] Briefly, full thickness donor skin grafts (1.5×1.5 cm^2) were prepared from the skin of IAGT treated and untreated homozygous E18 LAMB3^{IAP} mice or from E18 C57BL6 mice (as a technical control) and transferred to recipient sites on GFP transgenic mice. Recipient sites were created on the lateral thorax of the mice while carefully preserving the panniculus carnosus. The grafts were covered with petroleum gauze and held in place with a band-aid to create a pressure dressing. Dressings were removed after 5 days. Non-adherent grafts were considered technical failures and were excluded. Adherent grafts were monitored for signs of graft loss (hardening of the graft, and necrosis), and photographs were taken weekly. Grafts were considered lost when >90% of the surface area was necrotic and the graft hardened. The grafted skins were harvested 6 months after skin graft and analyzed by fluorescent stereomicroscopy and immunohistochemistry for laminin-322 and GFP.

Statistical analysis

The data were analyzed by using the Fisher's exact test.

CONFLICT OF INTEREST

The authors declare no conflict of interest.

ACKNOWLEDGEMENTS

We thank Keith Alcorn (The Children's Hospital of Philadelphia) for animal support, Ray Meade (The Biomedical Imaging Core/Electron Microscopy Resource Laboratory of the University of Pennsylvania) for electron microscopy support and Xiaohua Chen (The Children's Hospital of Philadelphia) for qPCR support. These studies were supported by NIH/NIAMS Grant R01 AR54876 (JU) and by funds from the Department of Surgery and the Ruth and Tristram C Colket Chair in Pediatric Surgery, Children's Hospital of Philadelphia (AWF).

1 Mavilio F, Pellegrini G, Ferrari S, Di Nunzio F, Di Iorio E, Recchia A *et al.* Correction of junctional epidermolysis bullosa by transplantation of genetically modified epidermal stem cells. *Nat Med* 2006; **12**: 1397–1402.
2 Remington J, Wang X, Hou Y, Zhou H, Burnett J, Muirhead T *et al.* Injection of recombinant human type VII collagen corrects the disease phenotype in a murine model of dystrophic epidermolysis bullosa. *Mol Ther* 2009; **17**: 26–33.
3 Wagner JE, Ishida-Yamamoto A, McGrath JA, Hordinsky M, Keene DR, Woodley DT *et al.* Bone marrow transplantation for recessive dystrophic epidermolysis bullosa. *N Engl J Med* 2010; **363**: 629–639.
4 Wong T, Gammon L, Liu L, Mellerio JE, Dopping-Hepenstal PJ, Pacy J *et al.* Potential of fibroblast cell therapy for recessive dystrophic epidermolysis bullosa. *J Invest Dermatol* 2008; **128**: 2179–2189.
5 Uitto J, McGrath JA, Rodeck U, Bruckner-Tuderman L, Robinson EC. Progress in epidermolysis bullosa research: toward treatment and cure. *J Invest Dermatol* 2010; **130**: 1778–1784.
6 Chino T, Tamai K, Yamazaki T, Otsuru S, Kikuchi Y, Nimura K *et al.* Bone marrow cell transfer into fetal circulation can ameliorate genetic skin diseases by providing fibroblasts to the skin and inducing immune tolerance. *Am J Pathol* 2008; **173**: 803–814.
7 Tolar J, Ishida-Yamamoto A, Riddle M, McElmurry RT, Osborn M, Xia L *et al.* Amelioration of epidermolysis bullosa by transfer of wild-type bone marrow cells. *Blood* 2009; **113**: 1167–1174.
8 Muhle C, Jiang QJ, Charlesworth A, Bruckner-Tuderman L, Meneguzzi G, Schneider H. Novel and recurrent mutations in the laminin-5 genes causing lethal junctional epidermolysis bullosa: molecular basis and clinical course of Herlitz disease. *Hum Genet* 2005; **116**: 33–42.
9 Laimer M, Lanschuetzer CM, Diem A, Bauer JW. Herlitz junctional epidermolysis bullosa. *Dermatol Clin* 2010; **28**: 55–60.
10 Zanjani ED, Anderson WF. Prospects for *in utero* human gene therapy. *Science* 1999; **285**: 2084–2088.
11 Schneider H, Coutelle C. *In utero* gene therapy: the case for. *Nat Med* 1999; **5**: 256–257.
12 Douar AM, Adebakin S, Themis M, Pavirani A, Cook T, Coutelle C. Foetal gene delivery in mice by intra-amniotic administration of retroviral producer cells and adenovirus. *Gene Therapy* 1997; **4**: 883–890.
13 Waddington SN, Buckley SM, Bernloehr C, Bossow S, Ungerechts G, Cook T *et al.* Reduced toxicity of F-deficient Sendai virus vector in the mouse fetus. *Gene Therapy* 2004; **11**: 599–608.
14 Sato M, Tanigawa M, Kikuchi N. Nonviral gene transfer to surface skin of mid-gestational murine embryos by intraamniotic injection and subsequent electroporation. *Mol Reprod Dev* 2004; **69**: 268–277.
15 Yoshizawa J, Li XK, Fujino M, Kimura H, Mizuno R, Hara A *et al.* Successful *in utero* gene transfer using a gene gun in midgestational mouse fetuses. *J Pediatr Surg* 2004; **39**: 81–84.
16 Muhle C, Neuner A, Park J, Pacho F, Jiang Q, Waddington SN *et al.* Evaluation of prenatal intra-amniotic LAMB3 gene delivery in a mouse model of Herlitz disease. *Gene Therapy* 2006; **13**: 1665–1676.
17 Endoh M, Koibuchi N, Sato M, Morishita R, Kanzaki T, Murata Y *et al.* Fetal gene transfer by intrauterine injection with microbubble-enhanced ultrasound. *Mol Ther* 2002; **5**: 501–508.
18 Ito M, Liu Y, Yang Z, Nguyen J, Liang F, Morris RJ *et al.* Stem cells in the hair follicle bulge contribute to wound repair but not to homeostasis of the epidermis. *Nat Med* 2005; **11**: 1351–1354.
19 Levy V, Lindon C, Harfe BD, Morgan BA. Distinct stem cell populations regenerate the follicle and interfollicular epidermis. *Dev Cell* 2005; **9**: 855–861.

20 Cotsarelis G, Sun TT, Lavker RM. Label-retaining cells reside in the bulge area of pilosebaceous unit: implications for follicular stem cells, hair cycle, and skin carcinogenesis. *Cell* 1990; **61**: 1329–1337.
21 Fuchs E, Tumbar T, Guasch G. Socializing with the neighbors: stem cells and their niche. *Cell* 2004; **116**: 769–778.
22 Lavker RM, Sun TT. Epidermal stem cells: properties, markers, and location. *Proc Natl Acad Sci USA* 2000; **97**: 13473–13475.
23 Byrne C, Hardman M, Nield K. Covering the limb–formation of the integument. *J Anat* 2003; **202**: 113–123.
24 Endo M, Zoltick PW, Peranteau WH, Radu A, Muvarak N, Ito M *et al.* Efficient *in vivo* targeting of epidermal stem cells by early gestational intraamniotic injection of lentiviral vector driven by the keratin 5 promoter. *Mol Ther* 2008; **16**: 131–137.
25 Kuster JE, Guarnieri MH, Ault JG, Flaherty L, Swiatek PJ. IAP insertion in the murine LamB3 gene results in junctional epidermolysis bullosa. *Mamm Genome* 1997; **8**: 673–681.
26 Endo M, Zoltick PW, Chung DC, Bennett J, Radu A, Muvarak N *et al.* Gene transfer to ocular stem cells by early gestational intraamniotic injection of lentiviral vector. *Mol Ther* 2007; **15**: 579–587.
27 Henriques-Coelho T, Gonzaga S, Endo M, Zoltick PW, Davey M, Leite-Moreira AF *et al.* Targeted gene transfer to fetal rat lung interstitium by ultrasound-guided intrapulmonary injection. *Mol Ther* 2007; **15**: 340–347.
28 Kim MG, Lee G, Lee SK, Lolkema M, Yim J, Hong SH *et al.* Epithelial cell-specific laminin 5 is required for survival of early thymocytes. *J Immunol* 2000; **165**: 192–201.
29 Aumailley M, Smyth N. The role of laminins in basement membrane function. *J Anat* 1998; **193** (Pt 1): 1–21.
30 Stanley JR, Rubinstein N, Klaus-Kovtun V. Epidermolysis bullosa acquisita antigen is synthesized by both human keratinocytes and human dermal fibroblasts. *J Invest Dermatol* 1985; **85**: 542–545.
31 Woodley DT, Krueger GG, Jorgensen CM, Fairley JA, Atha T, Huang Y *et al.* Normal and gene-corrected dystrophic epidermolysis bullosa fibroblasts alone can produce type VII collagen at the basement membrane zone. *J Invest Dermatol* 2003; **121**: 1021–1028.
32 Amano S, Nishiyama T, Burgeson RE. A specific and sensitive ELISA for laminin 5. *J Immunol Methods* 1999; **224**: 161–169.
33 Hata D, Miyazaki M, Seto S, Kadota E, Muso E, Takasu K *et al.* Nephrotic syndrome and aberrant expression of laminin isoforms in glomerular basement membranes for an infant with Herlitz junctional epidermolysis bullosa. *Pediatrics* 2005; **116**: e601–e607.
34 Laimer M, Lanschützer CM, Nischler E, Klausegger A, Diem A, Pohla-Gubo G *et al.* [Hereditary blistering diseases. Symptoms, diagnosis and treatment of epidermolysis bullosa]. *Hautarzt* 2009; **60**: 378–388.
35 Endo M, Henriques-Coelho T, Zoltick PW, Stitelman DH, Peranteau WH, Radu A *et al.* The developmental stage determines the distribution and duration of gene expression after early intra-amniotic gene transfer using lentiviral vectors. *Gene Therapy* 2010; **17**: 61–71.
36 Sakai N, Waterman EA, Nguyen NT, Keene DR, Marinkovich MP. Observations of skin grafts derived from keratinocytes expressing selectively engineered mutant laminin-332 molecules. *J Invest Dermatol* 2010; **130**: 2147–2150.
37 Stitelman DH, Endo M, Bora A, Muvarak N, Zoltick PW, Flake AW *et al.* Robust *in vivo* transduction of nervous system and neural stem cells by early gestational intra amniotic gene transfer using lentiviral vector. *Mol Ther* 2010; **18**: 1615–1623.
38 Uitto J, Pfendner E, Jackson LG. Probing the fetal genome: progress in non-invasive prenatal diagnosis. *Trends Mol Med* 2003; **9**: 339–343.
39 Weissman A, Itskovitz-Eldor J, Jakobi P. Sonographic measurement of amniotic fluid volume in the first trimester of pregnancy. *J Ultrasound Med* 1996; **15**: 771–774.
40 Matsui C, Wang CK, Nelson CF, Bauer EA, Hoeffler WK. The assembly of laminin-5 subunits. *J Biol Chem* 1995; **270**: 23496–23503.
41 Reynolds ES. The use of lead citrate at high pH as an electron-opaque stain in electron microscopy. *J Cell Biol* 1963; **17**: 208–212.
42 Qin XF, An DS, Chen IS, Baltimore D. Inhibiting HIV-1 infection in human T cells by lentiviral-mediated delivery of small interfering RNA against CCR5. *Proc Natl Acad Sci USA* 2003; **100**: 183–188.
43 Kaufman CK, Sinha S, Bolotin D, Fan J, Fuchs E. Dissection of a complex enhancer element: maintenance of keratinocyte specificity but loss of differentiation specificity. *Mol Cell Biol* 2002; **22**: 4293–4308.
44 Nakano A, Chao SC, Pulkkinen L, Murrell D, Bruckner-Tuderman L, Pfendner E *et al.* Laminin 5 mutations in junctional epidermolysis bullosa: molecular basis of Herlitz vs non-Herlitz phenotypes. *Hum Genet* 2002; **110**: 41–51.
45 Billingham RE, Krohn PL, Medawar PB. Effect of cortisone on survival of skin homografts in rabbits. *Br Med J* 1951; **1**: 1157–1163.

The FASEB Journal • Research Communication

HIG1, a novel regulator of mitochondrial γ-secretase, maintains normal mitochondrial function

Hiroki Hayashi,* Hironori Nakagami,*,†,[1] Makiko Takeichi,* Munehisa Shimamura,†,‡ Nobutaka Koibuchi,§ Eiji Oiki,‖ Naoyuki Sato,‡ Hiroshi Koriyama,‡ Masaki Mori,* Rodriguez Gerardo Araujo,* Akito Maeda,¶ Ryuichi Morishita,† Katsuto Tamai,* and Yasufumi Kaneda*,[1]

*Division of Gene Therapy Science and †Division of Vascular Medicine and Epigenetics, United Graduate School of Child Development, ‡Division of Clinical Gene Therapy Science and ‖Center for Medical Research and Education, Graduate School of Medicine, and ¶Skin Regeneration, PIAS Collaborative Research, The Center for Advanced Science and Innovation, Osaka University, Osaka Japan; and §Department of Advanced Clinical Sciences and Therapeutics, Graduate School of Medicine, The University of Tokyo, Tokyo, Japan

ABSTRACT **The γ-secretase complex (which contains presenilins, nicastrin, anterior pharynx defective-1, and presenilin enhancer-2) cleaves type I transmembrane proteins, including Notch and amyloid precursor protein. Dysregulated γ-secretase activity has been implicated in the pathogenesis of Alzheimer's disease, stroke, atherosclerosis, and cancer. Tight regulation of γ-secretase activity is required for normal physiology. Here, we isolated HIG1 (hypoxia inducible gene 1, domain member 1A) from a functional screen of γ-secretase inhibitory genes. HIG1 was highly expressed in the brain. Interestingly, HIG1 was localized to the mitochondria and was directly bound to γ-secretase components on the mitochondrial membrane in SK-N-SH neuroblastoma cells. Overexpresssion of HIG1 attenuated hypoxia-induced γ-secretase activation on the mitochondrial membrane and the accumulation of intracellular amyloid β. This accumulation was accompanied by hypoxia-induced mitochondrial dysfunction. The latter half domain of HIG1 was required for binding to the γ-secretase complex and suppression of γ-secretase activity. Moreover, depletion of HIG1 increased γ-secretase activation and enhanced hypoxia-induced mitochondrial dysfunction. In summary, HIG1 is a novel modulator of the mitochondrial γ-secretase complex, and may play a role in the maintenance of normal mitochondrial function.—Hayashi, H., Nakagami, H., Takeichi, M., Shimamura, M., Koibuchi, N., Oiki, E., Sato, N., Koriyama, H., Mori, M., Gerardo Araujo, R., Maeda, A., Morishita, R., Tamai, K., Kaneda, Y. HIG1, a novel regulator of mitochondrial γ-secretase, maintains normal mitochondrial function. *FASEB J.* 26, 2306–2317 (2012). www.fasebj.org**

Key Words: Alzheimer's disease · hypoxia · neuron · oxidative stress · intracellular Aβ

THE γ-SECRETASE COMPLEX cleaves the transmembrane domains of several type 1 transmembrane proteins, including Notch and amyloid precursor protein (APP). Abnormal γ-secretase activity is associated with the development of Alzheimer's disease (1), stroke (2), atherosclerosis (3), and cancer (4). The γ-secretase complex is a high-molecular-weight complex that consists of 4 proteins: presenilin (PS), nicastrin (NCT), anterior pharynx defective 1 (APH1), and presenilin enhancer 2 (PEN2) (5, 6). Whereas this complex is required for γ-secretase activity, other factors also are involved in the modulation of γ-secretase activity (7, 8). For instance, CD147, a transmembrane glycoprotein with 2 Ig-like domains, reduced the production of amyloid β (Aβ) by acting as a suppressor of the γ-secretase complex at the plasma membrane (9). TMP21, a member of the p24 cargo protein family, decreases γ-secretase activity through an interaction between the complex and its transmembrane domain (10). The identification of novel γ-secretase modulators might explain the tissue-specific differences in γ-secretase activity and indicate novel therapeutic targets for the diseases mentioned above.

Abbreviations: Aβ, amyloid β; APH1, anterior pharynx defective 1; APP, amyloid precursor protein; BACE, β-secretase; co-IP, coimmunoprecipitation; COXIV, cytochrome *c* oxydase; FACL4, long-chain fatty acid CoA synthase; FHL2, 4½ LIM protein 2; GSI, γ-secretase inhibitor; HEK, human embryonic kidney; HIG1, hypoxia-inducible gene 1 domain member 1A; IDE, insulin-degrading enzyme; MAM, mitochondria-associated ER membrane; MCAo, middle cerebral artery occlusion; NCT, nicastrin; PEN2, presenilin enhancer 2; PREP, presequence peptidase; PS, presenilin; RasGAP, Ras GTPase-activating protein; ROS, reactive oxygen species

[1] Correspondence: Division of Gene Therapy Science, Graduate School of Medicine, Osaka University, 2-2 Yamadaoka, Suita, Osaka 565-0871, Japan. E-mail: Y.K., kaneday@gts.med.osaka-u.ac.jp; H.N., nakagami@gts.med.osaka-u.ac.jp

doi: 10.1096/fj.11-196063

This article includes supplemental data. Please visit *http://www.fasebj.org* to obtain this information.

0892-6638/12/0026-2306 © FASEB

In this study, we screened a human adult heart cDNA library using high-throughput screening to identify a novel γ-secretase regulatory component. We identified hypoxia-inducible gene 1 domain member A (HIG1), which regulates γ-secretase activity. We found that HIG1 was highly expressed in the heart, brain, and liver tissue, and colocalized with the γ-secretase complex on the mitochondrial membrane. Active γ-secretase complexes have been observed in various organelles, including the mitochondria (11), and the involvement of γ-secretase activity in mitochondrial function has been suggested by a recent article (12). Attention is currently focused on the relevance of γ-secretase activation and its relationship with mitochondrial dysfunction in several disorders (13). Therefore, we hypothesized that HIG1, a novel regulator of γ-secretase activity, is a potential therapeutic target for diseases that involve mitochondrial function.

MATERIALS AND METHODS

Cell culture, transfection, plasmids, and chemical reagents

The human neuroblastoma cell line, SK-N-SH (kindly provided by Dr. Nobutaka Okochi, Ehime University, Ehime, Japan), and human embryonic kidney (HEK) 293 were cultured in DMEM containing 10% FCS plus penicillin/streptomycin. The cells were grown at 37°C in a humidified 5% CO_2 incubator. Transfections of plasmid DNA were performed using Lipofectamine 2000 (Invitrogen, Grand Island, NY, USA) according to manufacturer's instructions. The APPswe (Swedish mutation) plasmid was used for transfections. The Swedish mutation of APP promotes Aβ production (14). To induce hypoxia, cells were placed in Ziploc bags (L&L, Tokyo, Japan) in the BBL GasPak plus anaerobic system (Becton Dickinson, Heidelberg, Germany), as described previously (15). The γ-secretase inhibitor (GSI), L-685,458, was obtained from the Peptide Institute (Osaka, Japan) and was used at 10 μM as a final concentration. Mitotracker, a mitochondria marker, was purchased from Molecular Probes (Invitrogen).

Subcellular fractionation

The subcellular fractionation procedure was performed as described previously (16). Briefly, cells were washed with cold PBS and suspended in chilled buffer (200 mM mannitol, 70 mM sucrose, 1 mM EGTA, and 10 mM HEPES, at pH 7.5). The cells were homogenized and centrifuged at 800 *g* for 5 min. The supernatant was centrifuged at 10,000 *g* for 10 min. The pellet contained the heavy membrane fraction. The supernatant was centrifuged at 100,000 × 30 min. The pellet formed after this centrifugation step contained the light membrane fraction, while the supernatant contained the cytosolic fraction.

Quantitative real-time PCR

Total RNA was extracted from mouse tissue (colon, liver, lung, heart, kidney, spleen, skeletal muscle, and brain) or rat brain with RNeasy Lipid Tissue Mini Kit (Qiagen, Valencia, CA, USA), according to the manufacturer's instructions. cDNAs were synthesized using the High-Capacity cDNA Reverse Transcription Kit (ABI, Foster City, CA, USA). The relative mRNA levels of HIG1 were quantified by real-time RT-PCR using the TaqMan Gene Expression Assay (mouse HIG1: Mm00787005; mouse β-actin: Mm02619580; rat HIG1: Rn00821654; rat β-actin: Rn00667869). The absolute number of gene copies was normalized against β-actin and was standardized to a sample standard curve.

Knockdown of HIG1 by miRNA interference

The miRNA expression vector, pcDNA6.2-GW/EmGFP-miR, containing a miRNA that targets the HIG1 mRNA, was designed by Invitrogen. The sequence of the miRNA was TGCTGTTTACAAGTTATATTCCATGCGTTTTGGCCACTGACTGACGCATGGAATAACTTGTAAA. As a control, pcDNA6.2-GW/EmGFP-miR-control-construct (Invitrogen), containing the sequences that are predicted not to target any known vertebrate genes, was used. The construct with the HIG1-targeting miRNA sequences or the control construct was transfected into SK-N-SH cells using Lipofectamine 2000 (Invitrogen).

Sandwich ELISA

Human Aβ(1-40) and Aβ(1-42) ELISA kits were obtained from Wako (Osaka, Japan). Sandwich ELISA was performed as described previously (17). Briefly, the medium culturing SK-N-SH cells was collected to quantify extracellular Aβ40 or Aβ42 with or without hypoxic stimulation. Then, cells were washed with chilled PBS twice and lysed. After 30 min of incubation, sonicated samples were centrifuged at 20,000 *g* for 5 min. Supernatant was subjected to sandwich ELISA to quantify intracellular Aβ40 or Aβ42. Procedure of sandwich ELISA was followed according to manufacturer's instructions.

Western blotting, coimmunoprecipitation (co-IP), and immunostaining

Western blotting and immunostaining were performed as described previously (18). Briefly, cell extracts were prepared in lysis buffer. Samples containing 10 μg of protein were separated on gradient gels, transferred to PVDF membranes (Hybond ECL; GE Healthcare, Little Chalfont, UK), and incubated at 4°C overnight with primary antibody anti-HIG-1 (0.5 μg/ml) and anti-PS1 (obtained from Millipore, Billerica, MA, USA); anti-NCT, anti-APP, and anti-Aβ (obtained from Cell Signaling Technology, Danvers, MA, USA); anti-APH1 (obtained from Thermo Scientific, Worcester, MA, USA); anti-PEN2 (obtained from Calbiochem, San Diego, CA, USA); anti-Ras GTPase-activating protein (RasGAP), anti-cytochrome *c* oxydase (COXIV), anti-insulin-degrading enzyme (IDE), and anti-β-secretase 1 (BACE1; obtained from Thermo Scientific); anti-HIF-1α and anti-presequence peptidase (PREP; obtained from Novus, Littleton, CO, USA); anti-M2 flag and anti-β-actin (obtained from Sigma, St. Louis, MO, USA); anti-long-chain fatty acid CoA synthase (FACL4; obtained from Santa Cruz Biotechnology, Santa Cruz, CA, USA); anti-caveolin1 (obtained from BD Biosciences, San Jose, CA, USA). The membranes were then washed and incubated with a 1:1000 dilution of mouse or rabbit horseradish peroxidase-conjugated IgG. Bound antibodies were detected by enhanced chemiluminescence (ECL; GE Healthcare) with Hyperfilm-MP (GE Healthcare). Co-IPs were performed in chilled buffer (20 mM HEPES, 150 mM KCl, and 2 mM EGTA) containing 1% CHAPSO as a solubilization detergent (11). Cell lysates were obtained from SK-N-SH or HEK 293 cells; after the protein concentrations were adjusted, the cell lysates were precleared for 60 min. After immunoprecipitation, the precipitated proteins were ana-

lyzed by Western blotting, as described above. For immunostaining, cells on glass coverslips were fixed in 4% paraformaldehyde for 15 min and permeabilized with 0.2% Triton X-100 for 2 min. After blocking in 5% skim milk, the samples were incubated with primary antibodies at 4°C overnight. The corresponding secondary antibodies were labeled with AlexaFluor 488 or 546 (1:1000; Molecular Probes, Eugene, OR, USA).

Surgical procedure

Male Wistar Rats (270 to 300 g; Charles River; Kanagawa, Japan) were used in this experiment. The right middle cerebral artery occlusion (MCAo) was performed by replacement of poly-L-lysine-coated 4- nylon, as described previously (19). *In situ* hybridization was performed as described previously (20). The cDNAs used for generation of Dig-labeled riboprobes were *HIG1* full sequence.

Antibody production

The monoclonal antibody against HIG1, ISK-MMH-TK1 (IgG1, κ), was generated by Ishihara Sangyo Kaisha (Osaka, Japan), as described in World Intellectual Property Organization patent application WO 2011/040429 A1. Briefly, an N-terminal cysteine adduct (20 aa, CMSTDTGVSLPSYEEDQGSK) of human HIG1 peptide (1–19 aa) was chemically synthesized and conjugated to a career protein (keyhole limpet hemocyanin). The N-terminal site 1–19 aa was selected as the most optimal site of the antigenic epitopes predicted by the BepiPred method (http://genome.cbs.dtu.dk/services/BepiPred/) comparing the variation of amino acid sequence between humans and mice.

The conjugation was injected into BALB/c mice for immunization. At 2 wk after the final booster, the spleen was extracted from the immunized mice, and spleen cells were fused with myeloma cells (X-63-Ag8.653) by HVJ Envelope (inactivated Sendai virus particle) Cell Fusion Kit GenomONE-CF (Ishihara Sangyo Kaisha). After performing a limiting dilution of the cells that produce the anti-HIG1 antibody, the supernatant of the culture medium containing the antibody (9.2 μg/ml) was used for immunostaining, Western blot, and IP, respectively, at 0.5, 0.5, and 1 μg/ml to detect endogenous HIG1. The dissociation constant (K_d) against recombinant human HIG1 protein was 2.2×10^{-10}M, as measured by competitive ELISA.

In vitro peptide cleavage assay for γ-secretase activity

The *in vitro* peptide cleavage assays were performed as described previously (21). Briefly, the subcellular fractions were lysed in hypotonic buffer (10 mM Tris-HCl, pH 7.4; 1 mM EDTA; and 1 mM EGTA) containing 0.2% CHAPS plus protease inhibitors (Roche, Basel, Switzerland). After the protein concentrations were determined, 10 μg of the protein was incubated at 37°C overnight with 10 μM of fluorescence-conjugated peptide substrate containing the γ-secretase cleavable sequence of APP, NMA-GGVVIATVK(DNP)-DRDRDR-NH_2 (Peptide Institute). The degree of substrate cleavage was measured at an excitation wavelength of 355 nm and an emission wavelength of 440 nm.

ATP measurement and reactive oxygen species (ROS) production

The intracellular ATP levels in SK-N-SH cells were determined with the CellTiter-Glo Luminescent Cell Viability Assay Kit (Promega, Madison, WI, USA), according to the manufacturer's instructions. The assay generates a luminescent signal produced by the luciferase reaction that is proportional to the amount of ATP present in the cells. ROS generation was detected using a fluorescence probe, mitoSOX, that detects mitochondrial superoxide production. Cells were pretreated with 5 μM mitoSOX at 37°C for 10 min.

Transmission electron microscopy

For electron microscopy, cells were fixed with 2.5% glutaraldehyde in 0.1 M phosphate buffer (pH7.4) at 4°C, and postfixed in 1% OsO_4 solution at 4°C for 1 h. The samples were then dehydrated in a graded concentration of ethanol and embedded in Quetol 812 epoxy resin (Nissin EM, Tokyo, Japan). Ultrathin sections (80 nm) were cut on a Reichert ultramicrotome (Ultracut E; Leica Microsystems, Wetzlar, Germany), stained with uranyl acetate and lead citrate, and examined with a Hitachi H-7100 electron microscope (Hitachi, Tokyo, Japan) at 75 kV (22).

Subcellular fractionation on sucrose gradient

Subcellular fractionation using sucrose gradient was performed as described previously (23). The homogenate was centrifuged at 1000 *g* for 20 min, then the supernatant was centrifuged again at 175,000 *g* for 30 min. After the pellet was homogenized, the homogenate was layered on the top of 10–45% sucrose gradient and centrifuged at 40,000 *g* for 60 min. Each fraction was collected from the top of tube and analyzed by immunoblotting.

Isolation and purification of mitochondria and mitochondria-associated ER membrane (MAM)

Isolation of mitochondria and MAM was performed as described previously (24). The crude mitochondrial fraction was obtained by differential centrifugation. Purified mitochondria and MAM were isolated from the crude mitochondrial fraction on Percoll gradients. Each fraction was analyzed by immunoblotting.

Statistical analysis

All values are expressed as means ± SD. Analysis of variance with subsequent Fisher's protected least significant difference test or the unpaired Student's *t* test were employed to determine the significance of multiple comparisons. All statistical analyses were performed using the Stat-View 5.0 software (SAS Institute, Inc., Cary, NC, USA). Values of $P < 0.05$ were considered statistically significant.

RESULTS

Functional screening for candidates of γ-secretase modulators

To identify candidate genes that inhibit γ-secretase activity, we screened a cDNA library from human adult heart tissue using our previously described functional screen (25). We repeated the screen 4 times; the first screen identified 189 genes, the second identified 40 genes, the third identified 12 genes, the fourth identified 2 genes. From the screen, 2 candidates were

selected: 4½ LIM protein 2 (FHL2; GenBank accession no. NM_001450), which is localized on chromosome 2, and HIG1 (GenBank NM_014056), which is localized on chromosome 3. Indeed, overexpression of FHL2 or HIG1 suppressed γ-secretase activity compared to the control (GFP overexpression) in the HEK 293 cell line (**Fig. 1*A***). In a co-IP assay, overexpressed Flag-HIG1 interacted with the γ-secretase components [presenilin1(PS1), nicastrin (NCT), anterior pharynx defective 1 (APH1) and presenilin enhancer 2 (PEN2), Fig. 1*B*], whereas overexpressed Flag-FHL2 did not interact with the γ-secretase components (data not shown), even though FHL2 was recently reported to be involved in the regulation of γ-secretase activity (26). Because HIG1 might regulate γ-secretase activity by direct binding, we focused on the analysis of HIG1.

HIG1 binds to γ-secretase complex on mitochondrial membrane

HIG1 was highly expressed in the brain, liver, and heart, and it was expressed at low levels in kidney and skeletal muscle (Supplemental Fig. S1*A*). Immunostaining analysis showed that endogenous HIG1 was localized to the mitochondria in SK-N-SH cells (Fig. 1*C*), which is consistent with a previous report (27), because HIG1 expression was merged with mitochondrial marker (Mitotracker), but not Golgi (GM130) or ER marker (calreticulin) (Fig. 1*D*). In the biochemical fractionation of cell membranes using sucrose density gradient assay, HIG1 was also expressed in same fraction of COXIV (mitochondrial marker), but not calreticulin (ER marker) or GM130 (Golgi marker), and partially matched with that of γ-secretase components (PS1, NCT, or APH1) (refs. 11, 28 and Fig. 1*E*). Moreover, in the analysis of subcellular fractionation analysis of heavy and light membrane fractions in SK-N-SH cells, HIG1 and γ-secretase components (PS1, NCT, or APH1) were expressed on the heavy membrane fraction, which contains mitochondrial membrane (Fig. 1*F*). We further separated the heavy membrane fraction into the purified mitochondria and mitochondria-associated ER, which was confirmed by FACL4 (24). As a result, HIG1 expression was observed in purified mitochondrial membrane, but not mitochondria-associated ER membrane (Fig. 1*G*).

We examined whether HIG1 can bind to γ-secretase complex in neuroblastoma cells by using some immunological and biochemical assays. Interestingly, endogenous HIG1 bound to the γ-secretase components (PS1, NCT, APH1 and PEN2) on mitochondrial membrane, but not in plasma membrane fraction (**Fig. 2*A*, *B***). Moreover, PS1, NCT, and APH1, which are γ-secretase components, were partially localized with HIG-1 in mitochondria by immunostaining analysis (Fig. 2*C* and Supplemental Fig. S1*B–D*). Similarly, as shown in Fig. 1*E*, the fraction of HIG1 expression was partially matched with that of PS1, NCT, or APH1. These results suggest that the HIG1/γ-secretase complex is located on the mitochondrial membrane, but not on the plasma membrane; next, we hypothesized that HIG1 might function as a specific γ-secretase inhibitor in the mitochondria.

HIG1 suppresses hypoxia-induced γ-secretase activity on mitochondria and is involved in intracellular Aβ production

The activity of the γ-secretase complex is up-regulated under hypoxic conditions in neuronal cells (29–31). Although hypoxic conditions have been shown to increase γ-secretase activity by up-regulating the expression of its components (*i.e.*, NCT and APH1; ref. 29), hypoxia did not increase HIG1 levels (Supplemental Fig. S2*A, B*). HIG1 expression was not also increased in the mitochondrial fraction (Supplemental Fig. S2*C, D*). Moreover, in the rat model of cerebral infarction, HIG1 mRNA expression was decreased at 24 or 72 h after MCAo by *in situ* hybridization (Fig. 2*D*) and real-time PCR (Fig. 2*E*). Thus, the discrepancy between γ-secretase activity and HIG expression might be bigger in *in vivo* hypoxic conditions. Cotreatment with a GSI attenuated mitochondrial dysfunction, including ROS generation and ATP production, which was accompanied by a decrease in intracellular Aβ production (12, 32). Enhanced expression levels of the γ-secretase components but not that of HIG1 during hypoxia led us to hypothesize that the hypoxia-induced mitochondrial γ-secretase activity causes mitochondrial dysfunction and subsequent neuronal death.

To test this hypothesis, we evaluated the hypoxia-induced γ-secretase activity in mitochondrial membranes of SK-N-SH cells that stably expressed HIG1. Although the expression levels of the γ-secretase components were unchanged (Supplemental Fig. S3*A*), an *in vitro* peptide cleavage assay demonstrated that the up-regulation of γ-secretase activity induced by hypoxia was inhibited in the mitochondrial fraction of cells that stably expressed HIG1 (50.8% decrease of up-regulation of γ-secretase activity compared to control, $P < 0.05$; **Fig. 3*A***), but not in the plasma membrane fraction (Supplemental Fig. S3*B*). Similarly, although Aβ40 was significantly increased in both intracellular and extracellular fractions under hypoxic condition, overexpressed HIG1 attenuated only intracellular Aβ40 accumulation (Fig. 3*B* and Supplemental Fig. S3*C*). Aβ42 was also increased under hypoxic conditions; however, the change was not obvious compared to Aβ40 (control, 1.17±0.01; HIG1, 1.17±0.01; hypoxia+control, 1.21±0.01; hypoxia +HIG1, 1.18±0.011; Supplemental Fig. S3*D*). On the other hand, the levels of intracellular Aβ-degrading enzymes, *i.e.*, IDE (33, 34) and PREP (35), were unchanged in cells that stably expressed HIG1 (Fig. 3*C*). In addition, overexpressed HIG1 did not change the levels of the APP processing enzyme, β-secretase, in either normal or hypoxic conditions (Fig. 3*D*). Overexpression of HIG1 did not affect the cleavage efficacy of γ-secretase on other substrates, such as Notch (Fig. 3*E*) and E-cadherin (Fig. 3*F*). The possibility that HIG1 acts as a substrate of γ-secretase

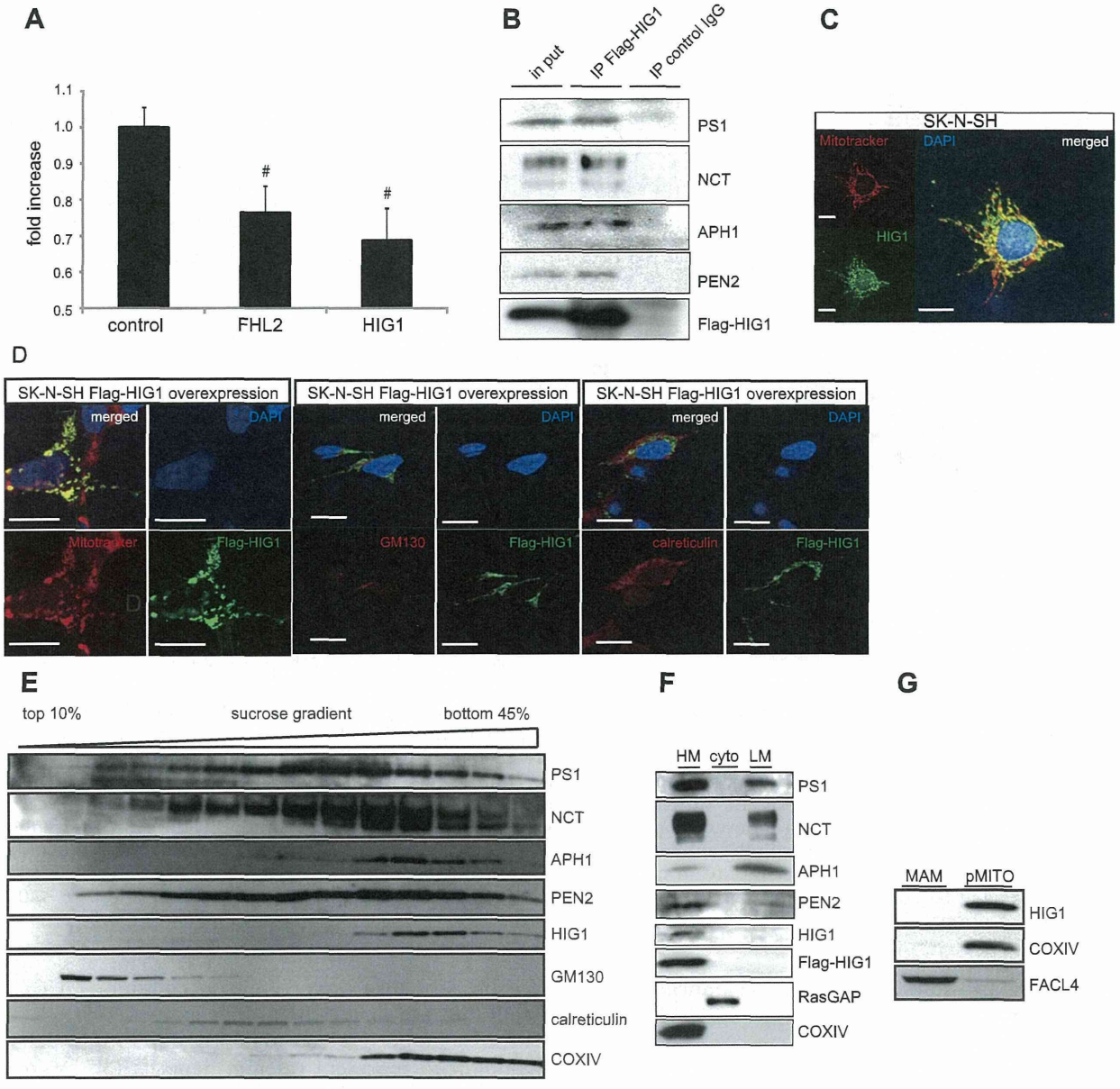

Figure 1. HIG1 was isolated from functional screening as a candidate of γ-secretase modulator and was localized on mitochondria. *A*) Quantification of γ-secretase activity by peptide cleavage assay in HEK 293 cells. Control indicates GFP transfection; FHL2 indicates FHL2 transfection; HIG1 indicates HIG1 transfection. $^{\#}P < 0.01$ *vs.* control; $n = 5$–7. *B*) γ-Secretase components (PS1, NCT, APH1, and PEN2) were coimmunoprecipitated with Flag-HIG1 following by immunoblot in HEK 293. IP Flag-HIG1 indicates immunoprecipitation with the anti-flag agarose. IP control IgG indicates immunoprecipitation with normal mouse IgG-AC. *C*) Immunostaining analysis of endogenous HIG1 and mitochondria (×400 view). Mitochondria were stained with Mitotracker (red). DAPI indicates nuclear staining (blue), HIG1 indicates staining with the anti-HIG1 antibody (green). Scale bars = 10 μm. *D*) Confocal images of Flag-HIG1 overexpressed SK-N-SH. DAPI indicates nuclear staining (blue), Flag-HIG1 indicates staining with the anti-Flag antibody (green). Cells were also stained with Mitotracker (red), anti-GM130 antibody (red), and anti-calreticulin antibody (red) as markers of mitochondria, Golgi body, and endoplasmic reticulum, respectively. Scale bars = 10 μm. *E*) Sucrose gradient analysis of the HIG1 and γ-secretase components (PS1, NCT, APH1, and PEN2) in membrane fraction. Each fraction was confirmed by immunoblotting with anti-GM130 antibody, anti-calreticulin antibody, and anti-COXIV antibody as markers of Golgi body, endoplasmic reticulum, and mitochondria, respectively. *F*) Subcellular fractionation of the overexpressed Flag-HIG1 and γ-secretase components (PS1, NCT, APH1, and PEN2) in cell membrane of SK-N-SH. HIG1 is expressed in heavy membrane (HM) fraction, but not light membrane (LM) and cytosolic fractions. RasGAP served as a cytosolic marker; COXIV served as a mitochondrial marker. *G*) Fractionation of mitochondria membrane into MAM and purified mitochondria (pMITO). HIG1 is expressed in pMITO, which is confirmed by immunoblotting with anti-FACL4 antibody.

was ruled out since HIG1 cleaved product was not detected under hypoxic conditions (Fig. 3*G*). These data indicated that hypoxia-induced γ-secretase activity at the mitochondrial membrane and intracellular Aβ production were suppressed by overexpression of HIG1.